



# Basin architecture controls on the chemical evolution and $^4\text{He}$ distribution of groundwater in the Paradox Basin

R.L. Tyne<sup>a,b,\*</sup>, P.H. Barry<sup>b</sup>, A. Cheng<sup>a</sup>, D.J. Hillegonds<sup>a</sup>, J.-H. Kim<sup>c</sup>, J.C. McIntosh<sup>c</sup>, C.J. Ballentine<sup>a</sup>

<sup>a</sup> Dept. of Earth Sci., University of Oxford, Oxford, UK

<sup>b</sup> Dept. of Marine Chem. and Geochem., Woods Hole Oceanographic Institution, Woods Hole, MA, USA

<sup>c</sup> Department of Hydrology and Atmospheric Sciences, University of Arizona, Tucson, AZ, USA



## ARTICLE INFO

### Article history:

Received 18 October 2021

Received in revised form 25 March 2022

Accepted 26 April 2022

Available online 11 May 2022

Editor: F. Moynier

### Keywords:

noble gases

helium

Paradox Basin

crustal fluid dating

groundwater migration

## ABSTRACT

Fluids such as  $^4\text{He}$ ,  $\text{H}_2$ ,  $\text{CO}_2$  and hydrocarbons accumulate within Earth's crust. Crustal reservoirs also have potential to store anthropogenic waste (e.g.,  $\text{CO}_2$ , spent nuclear fuel). Understanding fluid migration and how this is impacted by basin stratigraphy and evolution is key to exploiting fluid accumulations and identifying viable storage sites. Noble gases are powerful tracers of fluid migration and chemical evolution, as they are inert and only fractionate by physical processes. The distribution of  $^4\text{He}$ , in particular, is an important tool for understanding diffusion within basins and for groundwater dating. Here, we report noble gas isotope and abundance data from 36 wells across the Paradox Basin, Colorado Plateau, USA, which has abundant hydrocarbon,  $^4\text{He}$  and  $\text{CO}_2$  accumulations. Both groundwater and hydrocarbon samples were collected from 7 stratigraphic units, including within, above and below the Paradox Formation (P.Fm) evaporites. Air-corrected helium isotope ratios ( $0.0046 - 0.127 R_A$ ) are consistent with radiogenic overprinting of predominantly groundwater-derived noble gases. The highest radiogenic noble gas concentrations are found in formations below the P.Fm. Atmosphere-derived noble gas signatures are consistent with meteoric recharge and multi-phase interactions both above and below the P.Fm, with greater groundwater-gas interactions in the shallower formations. Vertical diffusion models, used to reconstruct observed groundwater helium concentrations, show the P.Fm evaporite layer to be effectively impermeable to helium diffusion and a regional barrier for mobile elements but, similar to other basins, a basement  $^4\text{He}$  flux is required to accumulate the  $^4\text{He}$  concentrations observed beneath the P.Fm. The verification that evaporites are regionally impermeable to diffusion, of even the most diffusive elements, is important for sub-salt helium and hydrogen exploration and storage, and a critical parameter in determining  $^4\text{He}$ -derived mean groundwater ages. This is critical to understanding the role of basin stratigraphy and deformation on fluid flow and gas accumulation.

© 2022 The Author(s). Published by Elsevier B.V. This is an open access article under the CC BY license (<http://creativecommons.org/licenses/by/4.0/>).

## 1. Introduction

The hydrogeology and hydrogeochemistry of sedimentary basins are inherently complex due to their stratigraphic, structural and temporal controls. Therefore it is critical to understand both the present-day and paleo-fluid flow and geochemistry of a basin, which can inform us about lateral and vertical fluid migration, interaction and emplacement. This is important in dating crustal fluids for groundwater resource security, identifying potential  $\text{CO}_2$  or nuclear waste disposal sites, and for helium and hydrogen explo-

ration (Torgersen, 1980; Hendry et al., 2005; Zhou and Ballentine, 2006; Cheng et al., 2021).

Noble gases are useful tools for investigating fluid migration within sedimentary basins. The three main terrestrial reservoirs of noble gases (atmosphere, crust, mantle) are isotopically distinct and therefore, the contribution from each to a particular sample can be readily determined (e.g., Ballentine et al., 2002). Noble gas abundance and isotope characteristics have been extensively used to constrain fluid provenance and migration (e.g., Ballentine et al., 1991, 2002; Gilfillan et al., 2008; Barry et al., 2016, 2018a, 2018b; Byrne et al., 2020). In addition, the distinct noble gas composition of various fluid sources in sedimentary basins have been used to identify and quantify the exchange between different subsurface fluid phases (e.g., Ballentine et al., 2002; Barry et al., 2016, 2018a; Byrne et al., 2020).

\* Corresponding author at: Dept. of Marine Chem. and Geochem., Woods Hole Oceanographic Institution, Woods Hole, MA, USA.

E-mail address: [Rebecca.tyne@whoi.edu](mailto:Rebecca.tyne@whoi.edu) (R.L. Tyne).

Helium, in particular, is an important noble gas as it is not only a valuable resource but can aid in dating crustal fluids.  $^4\text{He}$  is produced in-situ by the decay of U and Th in aquifer rocks and its concentration is a function of time and aquifer properties. Fluid residence time in sedimentary basin aquifers can be thus evaluated following (Eq. (1); Torgersen, 1980):

$$[^4\text{He}]_{\text{in-situ}} = \frac{\rho J(^4\text{He}) \Delta \varphi}{\varphi} \times t \quad (1)$$

where  $\rho$  is rock density ( $\text{g/cm}^3$ ),  $\varphi$  is porosity and  $t$  is ground-water residence time. The parameter  $\Delta$  defines the efficiency of helium transfer from mineral to groundwater;  $J(^4\text{He})$  is the production rate of  $^4\text{He}$  in aquifer minerals and is a function of the U and Th concentrations in the rock (Craig and Lupton, 1976). In practice,  $^4\text{He}$  accumulation rates in groundwater have large associated uncertainties, since knowledge of these rates depends on uncertain estimates of aquifer rock porosity, density, U/Th content, (diffusive) release rates of  $^4\text{He}$  from minerals, and aquifer heterogeneity along the integrated flow path of a water parcel in the subsurface (Torgersen, 1980). In addition, many crustal systems have acquired  $^4\text{He}$  from an external basement  $^4\text{He}$  flux (e.g., Torgersen and Clarke, 1985; Torgersen, 1989; Cheng et al., 2021). However, calculations of  $^4\text{He}$  residence times typically assume a constant external flux regardless of lithology and geographic location (e.g., Zhou and Ballentine, 2006; Barry et al., 2018a). Understanding the vertical and horizontal fluid migration within a basin can help constrain some of these uncertainties.

The Paradox Basin in the Colorado Plateau has a diverse and dynamic history of paleofluid flow, including widespread hydrocarbon,  $\text{CO}_2$  and He migration and accumulation (Fig. 1) (Nuccio and Condon, 1996; Gilfillan et al., 2008; Craddock et al., 2017). The basin is defined by the extent of a kilometer-thick Pennsylvanian evaporite confining unit (Paradox Formation, P.Fm), which has undergone diapirism (Hite and Buckner, 1981; Nuccio and Condon, 1996; Trudgill, 2011; Pederson et al., 2013), and separates the upper and lower basinal aquifer systems. The complex nature of the stratigraphy and fluid flow within the Paradox Basin, makes it an ideal location to investigate communication between hydrostratigraphic units (i.e., basinal aquifer systems) and the role of the basin architecture, including the presence of bedded and diapiric evaporites, on the chemical evolution of groundwater, which will have implications for both He exploration in the basin, waste storage and groundwater dating.

However, to date, there have been no systematic noble gas studies of both the Upper and Lower hydrostratigraphic units across the interior of the basin, despite questions remaining about the patterns and timescales of fluid circulation, migration of mantle derived gases (e.g.,  $\text{CO}_2$ ) and potential high He reservoirs (e.g., Dockrill and Shipton, 2010; Craddock et al., 2017; Crossey et al., 2006, 2009). In addition, the efficacy of salt as a regional barrier to gas diffusion in areas of faulting and with extensive salt 'tectonics' has not been investigated and could have significant implication for fluid dating as well as preserving potential exploitable reserves of helium/hydrogen. We present here noble gas isotope and abundance data from samples collected from groundwater and hydrocarbon wells across the Paradox Basin. Samples were taken from throughout the stratigraphic column from both below, within and above the P.Fm (Fig. 2) to investigate how the  $^4\text{He}$  distribution and associated noble gases is affected by the basin architecture (e.g., the widespread occurrence of an evaporite layer) and resulting subsurface fluid regime. Additionally, understanding how the  $^4\text{He}$  distribution is impacted by an evaporite layer has important implications for understanding basin-scale fluid flow and potential  $^4\text{He}$  reservoirs.

## 2. Geological background and hydrogeochemistry

The Paradox Basin is an approximately 85,000  $\text{km}^2$  eastward deepening flexural basin that developed in response to the Late Palaeozoic Uncompahgre Uplift of the ancestral Rocky Mountains (Hanshaw and Hill, 1969; Nuccio and Condon, 1996; Barbeau, 2003). The sedimentary rocks of the Paradox Basin overlie an early Proterozoic basement. A detailed geological history can be found in the SI.1.

There are three hydrostratigraphic units in the Paradox Basin, Upper (Post Paleozoic-Permian formations), Middle (Pennsylvanian P.Fm) and Lower (Devonian-Mississippian formations). The Lower hydrostratigraphic unit (below the P.Fm), containing the hydrocarbon-bearing McCracken Sandstone (Devonian) and Leadville Limestone (Mississippian) (Fig. 2), receives local meteoric recharge around the Abajo and La Sal mountains and margins of the salt anticlines (Hanshaw and Hill, 1969; Thackston et al., 1981). It has been hypothesized there is downward fluid flow throughout the basin based on a lower potentiometric surface of the Lower hydrostratigraphic unit compared to the Upper hydrostratigraphic unit, although the Lower unit is less affected by local topography (Hanshaw and Hill, 1969).

The Middle hydrostratigraphic unit (composed of the P.Fm) is a regional confining unit (Thackston et al., 1981; Hanshaw and Hill, 1969). The P.Fm is comprised of 1.8-2.5 km thick evaporites interbedded with dolomite and black shales (e.g., in the Desert Creek and Cane Creeks members), which are important hydrocarbon source rocks (Hite and Buckner, 1981; Nuccio and Condon, 1996; Trudgill, 2011). Following deposition, the P.Fm has undergone sediment loading and passive salt diapirism leading to a series of northwest-southeast trending salt walls and mini basins (e.g., Fig. 2) (Trudgill, 2011).

Notable formations to this study in the Upper hydrostratigraphic unit include the Cretaceous Burro Canyon Formation (Fm) (which forms the Burro Canyon Aquifer), Triassic Navajo and Entrada Fms (which form the Navajo Aquifer), Permian Cutler and Pennsylvanian Honaker Trail Fms (Fig. 2). During the Tertiary to Holocene (4-10 Ma; Lazear et al., 2011; Karlstrom et al., 2012; Murray et al., 2019), present day topographic gradients were formed through erosion of Cretaceous and Cenozoic formations, including the Mancos Shale (Nuccio and Condon, 1996), and incision of the Colorado River and its tributaries. The Laramide Orogeny and emplacement of related laccoliths aided in the creation of the higher topographic gradients. Groundwater flow in the Upper hydrostratigraphic unit (i.e., above the P.Fm) is mainly controlled by topography (Hanshaw and Hill, 1969; Thackston et al., 1981; King et al., 2014). Groundwater flow at the base of this unit directly dissolves evaporites in the underlying P.Fm (Kim et al., 2022).

Although there is no hydrogeological data, flow within the Precambrian basement is likely, given several hairline and open fractures and porosities which can exceed 9% (Bremkamp and Harr, 1988). Moreover, radiogenic strontium ( $^{87}\text{Sr}/^{86}\text{Sr}$  up to 0.735) from basinal fluid circulation through the basement rocks has previously been identified on the Colorado Plateau (Crossey et al., 2006; Kim et al., 2022).

Previous paleofluid studies in the Paradox Basin have focused primarily on the rock record, with inferences about paleofluid origin, composition, flowpaths and mixing (e.g., Beitler et al., 2003; Parry et al., 2004; Dockrill and Shipton, 2010). A recent study examined the hydrogeochemistry of fresh to saline formation waters across the hydrostatic units to constrain the fluid sources and geochemical evolution of paleofluids responsible for the sandstone bleaching and associated ore mineralisation within the Paradox Basin (Kim et al., 2022). They found dilution of connate brines and dissolution of evaporite minerals by meteoric waters in hydrostratigraphic units above and below the P.Fm. This occurred

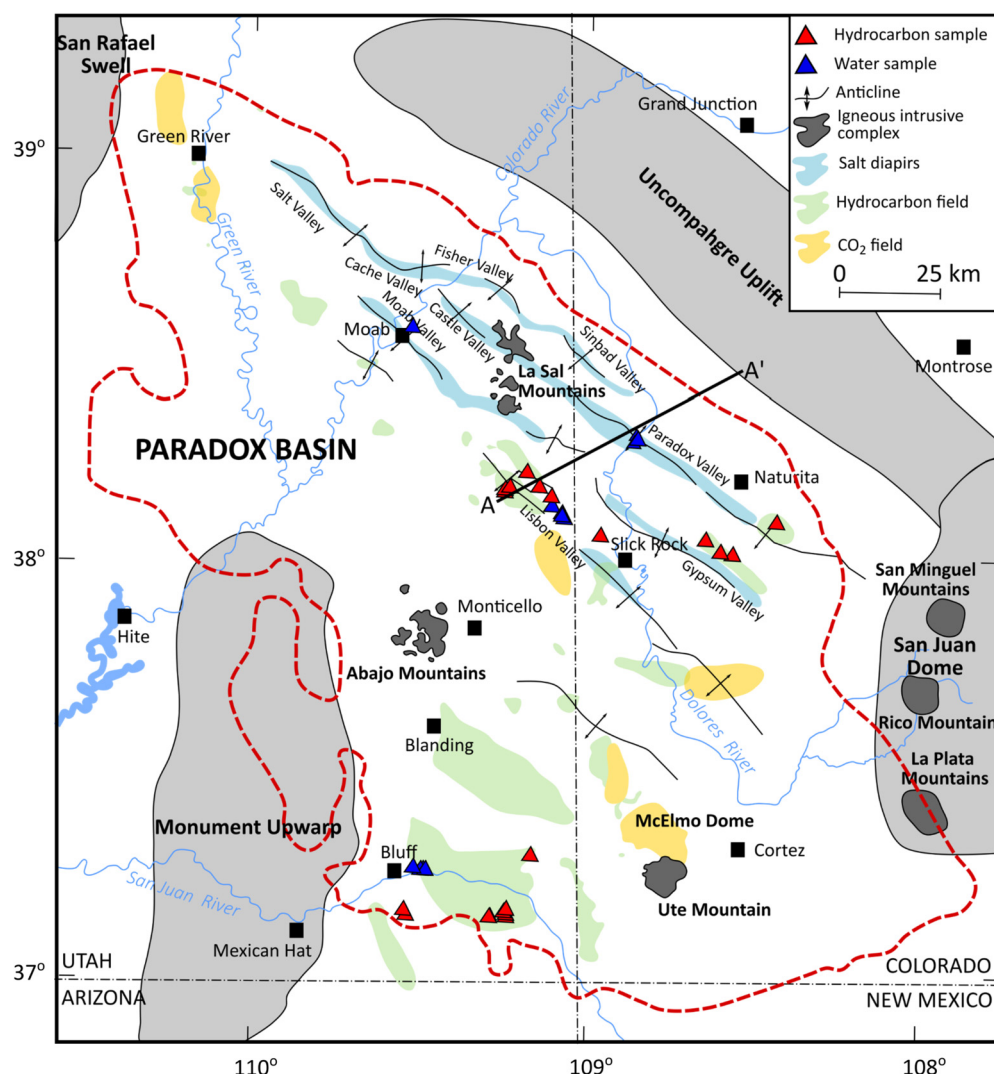


**Fig. 1.** Map of the study area, showing locations of water and hydrocarbon samples taken across the Paradox Basin. The cross section from A-A' can be found in Fig. 2. The map has been adapted from Harr (1996) and Kim et al. (2022).

during the past ~3–500 ka and >800 ka in the lower and upper hydrostratigraphic units, respectively based on  $^{14}\text{C}$  and  $^{81}\text{Kr}$  dating (Kim et al., 2021, 2022). They suggest recent erosion of the Mancos Shale confining unit and creation of higher topographic gradients, from incision of the Colorado Plateau starting ~10 to 4 Ma (Lazear et al., 2011; Karlstrom et al., 2012; Murray et al., 2019), enhanced deep meteoric water circulation and flushing of connate brines (Kim et al., 2021, 2022). Connate brines, formed from highly evaporated paleoseawater, have been retained within shale interbeds in the P.Fm, likely due to its low permeability, high salinity of fluids, and relatively short time period of meteoric flushing in adjacent aquifer systems (Ferguson et al., 2018; McIntosh and Ferguson, 2021; Kim et al., 2022).

Noble gases have previously been measured in gas fields around the exterior of the Paradox Basin on the Colorado Plateau, as well as at McElmo Dome in the southeast of the basin (Gilfillan et al., 2008; Craddock et al., 2017). These fields are either dominated by hydrocarbons,  $\text{CO}_2$  or  $\text{N}_2$ -He-Ar. The  $\text{N}_2$ -He-Ar rich fields are predominantly derived from crustal radiogenic production and are associated with structures and sutures in the Precambrian basement. The  $\text{CO}_2$ -rich fields (including McElmo Dome) have  $\text{CO}_2$  concentrations >75% and are magmatic in origin (Gilfillan et al., 2008; Craddock et al., 2017). Mantle  $\text{CO}_2$  and helium have also been observed in  $\text{CO}_2$  rich seeps across the Plateau (Crossey et al., 2006,

2009, 2016). Additionally, noble gases were measured in shallow groundwaters (Quaternary Valley Fill Aquifer and Lower Jurassic to Upper Triassic Glen Canyon Aquifer, Upper hydrostratigraphic unit) in the Moab and Spanish Valleys (northern Paradox Basin), to better understand the groundwater system, recharge sources and flow directions (Masbruch et al., 2019).

### 3. Methods

A total of 48 samples including 12 duplicates were taken from across 7 stratigraphic units in the Paradox Basin (Fig. 2, Table 1, Supplementary Table 1). Shallow groundwaters ( $n=15$ ) were collected from the Paradox Valley, Lisbon Valley and Greater Aneth Oil Field and 1 deep brine was collected from an artesian lithium exploration well in the Cane Creek member of the P.Fm. The groundwater samples from the Paradox Valley (Salt Diapir) are shallow brines (~14 m depth), formed by salt dissolution from meteoric circulation at the top of a salt wall, collected from brine extraction wells adjacent to the Dolores River. The remaining samples (11 produced gases, 8 casing gases (gases that exsolve and migrate up the well casing during production) and 1 produced fluid (condensate, water, gas mixture)) were taken from oil and gas fields across the basin (Fig. 1).

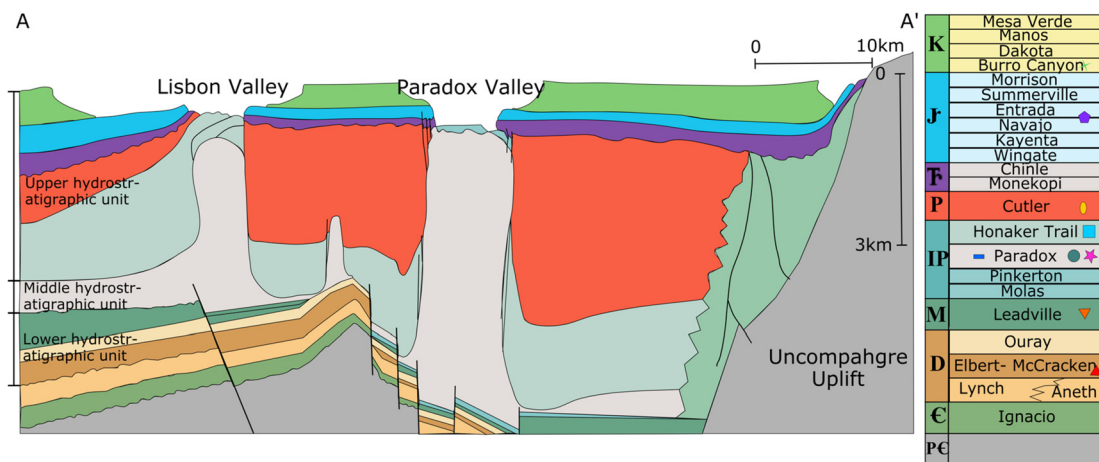


**Fig. 2.** Cross section of across part of the Paradox Basin (A-A', see Fig. 1), showing the variation in formation thickness across a subsection of the basin. Modified from Baars and Stevenson (1982), Baars (1996), King et al. (2014) and Kim et al. (2022). A simplified stratigraphic column for the Basin can be found to the right of the cross section (modified from Nuccio and Condon (1996)). Colours used within the cross section correspond to those in the stratigraphic column, and sampled formations are marked with symbols (used hereafter). (For interpretation of the colours in the figure(s), the reader is referred to the web version of this article.)

Water and produced fluid samples were collected in 3/8" refrigeration-grade copper tubes with stainless steel clamps following the methods described in Tyne et al. (2019). Casing gases were collected in Cu tubes using standard sampling methods (e.g., Barry et al., 2016). Noble gases were analysed in the Noble Laboratory at the University of Oxford, where there is a dedicated offline fluid extraction system, hydrocarbon extraction system and a purification line interfaced to two noble gas mass spectrometers. Full analytical procedures can be found in Tyne et al. (2019).

## 4. Results

All noble gas concentrations, isotope ratios and associated  $1\sigma$  errors are reported in Tables 1 and 2. Noble gas concentrations in the gas phase of produced fluids and casing gases have been shown to yield similar information about the subsurface system (Tyne et al., 2021). Therefore, for the produced fluid sample (MC 17-21), the concentration in the gas phase has been calculated following the methods in Tyne et al. (2019), assuming the different phases are at equilibrium, and hereafter is treated as a 'gas' phase sample. Due to solubility within elements being approximately the same for all isotopes, differences in the noble gas isotope ratios between the phases are expected to be negligible and therefore, the overall produced fluid, groundwater and gas phase ratios are directly comparable.

### 4.1. Helium

Measured helium isotopes ( $^3\text{He}/^4\text{He}$ ) are between 0.005 and  $0.79 R_A$  where  $R_A$  is the atmospheric ratio ( $R_A = 1.4 \times 10^{-6}$ ). Assuming all  $^{20}\text{Ne}$  is atmosphere derived, the  $^4\text{He}/^{20}\text{Ne}$  measured in the sample relative to the air value (0.32) for gas phase samples or air saturated water (ASW) (0.25 at  $10^\circ\text{C}$ , 0 M, 2000 m) for water phase samples can be used to calculate the atmospheric He contribution, which is then subtracted from the measured  $^3\text{He}/^4\text{He}$  (Hilton, 1996). When the  $^4\text{He}/^{20}\text{Ne}$  is high, the correction is negligible, however it can be significant when the measured  $^4\text{He}/^{20}\text{Ne}$  is close to air/ASW. Measured  $^4\text{He}/^{20}\text{Ne}$  in the samples range from  $2.95 \times 10^{-1}$  to  $1.71 \times 10^5$  and increase with depth with the shallowest samples having  $^4\text{He}/^{20}\text{Ne}$  closest to air/ASW (Supplementary Fig. 1). Where measured  $^4\text{He}/^{20}\text{Ne}$  are within error of the air/ASW, no correction is possible and we assume that all sample helium is atmosphere-derived. Air-corrected helium isotope ratios in the Paradox Basin range from 0.005 to  $0.127 R_A$  (Fig. 3). Low

$^3\text{He}/^4\text{He}$  are consistent with the majority of helium being derived from crustal radiogenic production.

Measured helium ( $^4\text{He}$ ) concentrations are between 0.044 and  $213 \times 10^{-6} \text{ cm}^3(\text{STP})/\text{g}_{\text{water}}$  in the water phase samples and between  $195$  to  $9,210 \times 10^{-6} \text{ cm}^3(\text{STP})/\text{cm}^3$  in the gas phase samples.

### 4.2. Neon

Measured  $^{20}\text{Ne}$  concentrations range from 0.084 to  $10.3 \times 10^{-7} \text{ cm}^3(\text{STP})/\text{g}_{\text{water}}$  in the water phase samples and from 0.090 to  $82.1 \times 10^{-7} \text{ cm}^3(\text{STP})/\text{cm}^3$  in the gas phase samples. Most samples have air-like neon isotopes ( $^{21}\text{Ne}/^{22}\text{Ne}=0.0290$ ,  $^{20}\text{Ne}/^{22}\text{Ne}=9.80$ ; Porcelli et al., 2002; Fig. 4). Deviations from air are a result of an excess in radiogenically produced  $^{21}\text{Ne}$  and  $^{22}\text{Ne}$  relative to air or due to mass fractionation effects (Young et al., 2002).

### 4.3. Argon, Krypton and Xenon

Argon isotope ratios ( $^{40}\text{Ar}/^{36}\text{Ar}$ ) range from 295 to 4,530. Apart from samples in the Navajo and Burro Canyon aquifers, there is excess radiogenic  $^{40}\text{Ar}$  ( $^{40}\text{Ar}^*$ ) relative to the air value (298.6, Lee et al., 2006). The amount of  $^{40}\text{Ar}^*$  relative to  $^{36}\text{Ar}$  is correlated with increasing  $^{21}\text{Ne}/^{22}\text{Ne}$  (Fig. 4b). The  $^{38}\text{Ar}/^{36}\text{Ar}$  ratios are between 0.139 and 0.224 and there is no correlation between  $^{38}\text{Ar}/^{36}\text{Ar}$  and  $^{20}\text{Ne}/^{22}\text{Ne}$ . Argon abundance ( $^{36}\text{Ar}$ ) ranges from  $0.027$  to  $3.28 \times 10^{-6} \text{ cm}^3(\text{STP})/\text{g}_{\text{water}}$  in the water phase samples and from  $0.025$  to  $5.5 \times 10^{-6} \text{ cm}^3(\text{STP})/\text{cm}^3$  in the gas phase samples.

Krypton ( $^{84}\text{Kr}$ ) concentrations within the gas phase samples range from  $0.32$  to  $7.38 \times 10^{-8} \text{ cm}^3(\text{STP})/\text{cm}^3$  and from  $0.101$  to  $9.53 \times 10^{-8} \text{ cm}^3(\text{STP})/\text{g}_{\text{water}}$  in the water phase. Xenon ( $^{130}\text{Xe}$ ) concentrations are between  $0.48$  to  $386 \times 10^{-10} \text{ cm}^3(\text{STP})/\text{cm}^3$  and  $0.12$  to  $5.68 \times 10^{-10} \text{ cm}^3(\text{STP})/\text{g}_{\text{water}}$  for the gas and water phase samples, respectively. The Kr and Xe isotope ratios are indistinguishable from air in all samples.

## 5. Discussion

In the following section we investigate the distribution of noble gases across the Paradox Basin to determine how basin architecture has influenced fluid migration pathways, which is key for both exploration and storage of  $\text{CO}_2$ ,  $\text{H}_2$  and nuclear waste. Our approach is to first determine the different fluid sources and their



**Table 1**Noble gas concentrations with 1 $\sigma$  errors. Measured noble gas concentrations are in cm<sup>3</sup>(STP)/cm<sup>3</sup> for the gas phase samples and cm<sup>3</sup>(STP)/g<sub>water</sub> for water phase samples.

Sample Name	Formation	<sup>4</sup> He ( $\times 10^{-6}$ )	$\pm$	<sup>20</sup> Ne ( $\times 10^{-7}$ )	$\pm$	<sup>36</sup> Ar ( $\times 10^{-6}$ )	$\pm$	<sup>84</sup> Kr ( $\times 10^{-8}$ )	$\pm$	<sup>130</sup> Xe ( $\times 10^{-10}$ )	$\pm$	<sup>3</sup> He/ <sup>4</sup> He	$\pm$	<sup>3</sup> He/ <sup>4</sup> He <sub>c</sub>	$\pm$
<b>Water phase (cm<sup>3</sup>(STP)/g<sub>water</sub>)</b>															
BOR 8E	Salt Diapir, Paradox	1.13	0.03	0.140	0.005	0.289	0.013	1.75	0.10	2.33	0.14	0.039	0.001	0.035	0.002
BOR 9E	Salt Diapir, Paradox	1.14	0.03	0.146	0.006	0.264	0.012	1.64	0.09	2.26	0.13	0.038	0.001	0.034	0.002
BOR 3E	Salt Diapir, Paradox	1.55	0.05	0.191	0.007	0.284	0.013	1.58	0.09	2.03	0.12	0.039	0.001	0.035	0.002
BOR 2E	Salt Diapir, Paradox	1.86	0.06	0.239	0.009	0.348	0.016	1.75	0.10	2.14	0.13	0.038	0.001	0.034	0.002
PW-4	Burro Canyon Aquifer	0.0443	0.0014	1.41	0.03	1.09	0.03	4.50	0.12	4.89	0.13	0.734	0.020		
PW-4 (dup)	Burro Canyon Aquifer	0.0449	0.0012	1.52	0.05	1.02	0.04	5.34	0.21	2.78	0.25	0.790	0.020		
PW-3	Burro Canyon Aquifer	0.0742	0.0023	1.82	0.04	1.19	0.03	4.70	0.12	4.89	0.13	0.614	0.017		
PW-12	Burro Canyon Aquifer	0.365	0.004	1.82	0.01	1.21	0.02	4.49	0.12	4.73	0.10	0.164	0.008	0.044	0.001
PW-8	Navajo Aquifer			1.91	0.04	1.26	0.03	5.02	0.13	5.27	0.14				
PW-8 (dup)	Navajo Aquifer	3.95	0.12	1.96	0.08	1.25	0.06	5.93	0.72	5.02	0.44	0.030	0.001	0.018	0.001
PW-11	Navajo Aquifer	0.586	0.018	1.78	0.04	1.08	0.03	4.25	0.11	4.43	0.12	0.092	0.003	0.016	0.001
PW-7	Navajo Aquifer	0.802	0.025	10.3	0.2	3.28	0.08	5.08	0.13	4.54	0.12	0.347	0.011	0.034	0.002
STCEC	Navajo Aquifer	0.899	0.027	2.59	0.1	1.49	0.07	5.32	0.65	5.68	0.49	0.132	0.003	0.064	0.005
BWC-1	Navajo Aquifer	0.759	0.023	2.72	0.06	1.52	0.04	3.24	0.08	3.38	0.09	0.206	0.008	0.127	0.008
BWC-2	Navajo Aquifer	3.46	0.11	2.50	0.05	1.46	0.04	3.18	0.08	3.35	0.09	0.141	0.004	0.126	0.006
BWC-3	Navajo Aquifer	8.26	0.25	2.40	0.09	1.41	0.06	6.15	0.75	5.47	0.48	0.099	0.002	0.093	0.005
TRTP	Navajo Aquifer	18.5	0.6	2.24	0.09	1.26	0.06	9.53	1.16	4.83	0.42	0.093	0.002	0.090	0.005
Cane Creek	Cane Creek Mbr, Paradox	213	2	0.0835	0.0010	0.0267	0.0005	0.101	0.002	0.118	0.010	0.0046	0.0002	0.0046	0.0001
<b>Gas Phase (cm<sup>3</sup>(STP)/cm<sup>3</sup>)</b>															
AM-75	Cutler	478	16	36.8	1.5	4.86	0.08	6.92	0.13	3.39	0.16	130	0.041	0.003	0.038
AM-62	Cutler	1360	40	36.2	1.4	5.50	0.08	7.38	0.14	3.86	0.19	376	0.039	0.001	0.039
AM-11-E34	Cutler-Honaker Trail	705	20	2.87	0.11	0.409	0.007	0.691	0.013	0.559	0.027	2460	0.031	0.002	0.031
MM 31-42	Honaker Trail	1280	80	6.11	0.043	1.43	0.10	0.993	0.049	0.963	0.052	0.011	0.001	0.011	0.001
MM 31-42 (dup)	Honaker Trail	1270	80									0.013	0.002	0.013	0.002
BI 24-31	Honaker Trail	1300	80	5.43	0.29			0.587	0.029	0.476	0.026	0.055	0.002	0.054	0.005
BI 24-31 (dup)	Honaker Trail	1660	100									0.058	0.002		
BH 10-31	Honaker Trail	261	9	27.3	1.1	3.70	0.06	5.39	0.10	2.95	0.14	0.025	0.001	0.022	0.001
HC 31-31	Honaker Trail	405	13	15.3	0.6	2.68	0.04	4.73	0.09	2.62	0.13	0.009	0.001	0.008	0.001
FF-2-19	Honaker Trail	1530	50	2.97	0.12	0.455	0.007	0.918	0.017	1.05	0.05	0.038	0.002	0.038	0.002
FF-2-19 (dup)	Honaker Trail	1500	50	3.34	0.12	0.499	0.013	1.03	0.05	0.985	0.018	0.035	0.001	0.035	0.002
Tohonalda 35-B	Desert Creek Mbr, Paradox	515	17	0.147	0.003							0.070	0.002	0.070	0.002
Tohonalda 1	Desert Creek Mbr, Paradox	304	10	0.121	0.005	0.0612	0.0014	0.327	0.006	0.608	0.029	0.067	0.003	0.067	0.004
Tohonalda 1 (dup)	Desert Creek Mbr, Paradox	301	10									0.073	0.004		
Anasazi 1	Desert Creek Mbr, Paradox	256	8	0.0994	0.0040	0.0620	0.0020	0.338	0.006	0.725	0.035	0.029	0.002	0.029	0.002
Sahgzie 1	Desert Creek Mbr, Paradox	230	8	0.0902	0.0036	0.0616	0.0015	0.321	0.006	0.678	0.033	0.025	0.003	0.025	0.002
Sahgzie 1 (dup)	Desert Creek Mbr, Paradox	244	8									0.030	0.003		
Monument-8N-2	Desert Creek Mbr, Paradox	242	8	0.138	0.005	0.0538	0.0014	0.281	0.005	0.572	0.028	0.011	0.001	0.011	0.001
Monument-8N-2 (dup)	Desert Creek Mbr, Paradox	239	8									0.012	0.001		
WM 22-43	Desert Creek Mbr, Paradox	235	8	0.296	0.012	0.178	0.003	0.746	0.014	1.12	0.05	0.024	0.002	0.024	0.002
WM 22-43 (dup)	Desert Creek Mbr, Paradox	238	8			0.273	0.007	0.863	0.044	1.16	0.02	0.029	0.001	0.0290	0.0010
WM 34-31	Desert Creek Mbr, Paradox	195	6	0.293	0.012	0.228	0.004	0.637	0.012	0.994	0.048	0.021	0.002	0.021	0.002
WM 34-31 (dup)	Desert Creek Mbr, Paradox	197	6	0.347	0.014	0.181	0.003	0.642	0.012	1.01	0.05	0.027	0.002	0.027	0.002
WM 34-33	Desert Creek Mbr, Paradox	213	7	0.484	0.019	0.296	0.005	1.24	0.02	1.65	0.08	0.030	0.001	0.0254	0.0020
McIntyre 17-21	Mississippian	1880	110	0.239	0.015	0.119	0.008	0.477	0.031	0.11	0.01	0.034	0.001	0.034	0.003
Lisbon D8-10	Mississippian- Devonian	8970	550			0.120	0.009	0.329	0.016	0.57	0.03	0.046	0.001		
Lisbon 10-33	Devonian	3600	120	0.211	0.008	0.109	0.002	0.614	0.011	1.35	0.06	0.042	0.001	0.042	0.003
Lisbon 10-33 (dup)	Devonian	3540	120	0.209	0.008	0.104	0.003	0.617	0.011	1.34	0.06	0.042	0.001	0.042	0.003
Lisbon B8-10	Devonian	9210	560	0.709	0.038	0.212	0.014	0.939	0.046	1.49	0.08	0.041	0.001	0.041	0.004
Lisbon B8-10 (dup)	Devonian					0.197	0.005	0.893	0.046	1.32	0.02				

**Table 2**

Noble gas isotope and elemental ratios and associated  $1\sigma$  errors.  $^3\text{He}/^4\text{He}$  ratios are given relative to air ( $1.4 \times 10^{-6}$ ).  $^3\text{He}/^4\text{He}_c$  is corrected for the atmospheric component (following methods in Hilton (1996)).

Sample Name	$^{21}\text{Ne}/^{22}\text{Ne}$	$\pm$	$^{20}\text{Ne}/^{22}\text{Ne}$	$\pm$	$^{40}\text{Ar}/^{36}\text{Ar}$	$\pm$	$^{38}\text{Ar}/^{36}\text{Ar}$	$\pm$
<b>Water phase</b>								
BOR well 8E	0.02955	0.00026	9.59	0.07	303	2	0.198	0.005
BOR well 9E	0.02946	0.00026	9.56	0.07	304	2	0.199	0.005
BOR well 3E	0.02930	0.00025	9.53	0.07	302	2	0.198	0.005
BOR well 2E	0.02934	0.00026	9.53	0.07	302	2	0.199	0.005
PW-4	0.02966	0.00001	9.73	0.02	298	2	0.194	0.006
PW-4 (dup)	0.02873	0.00008	9.80	0.01	299	2	0.190	0.002
PW-3	0.02966	0.00001	9.82	0.02	299	2	0.195	0.006
PW-12	0.02965	0.00003	9.83	0.02	298	2	0.195	0.006
PW-8	0.02967	0.00002	9.77	0.02	299	2	0.195	0.006
PW-8 (dup)	0.02953	0.00006	9.84	0.01	299	1	0.181	0.006
PW-11	0.02968	0.00002	9.74	0.02	299	2	0.194	0.006
PW-7	0.02963	0.00002	9.81	0.02	298	2	0.194	0.006
STCEC	0.02952	0.00010	9.84	0.01	298	1	0.197	0.007
BWC-1	0.02965	0.00002	9.82	0.02	298	2	0.195	0.006
BWC-2	0.02967	0.00002	9.82	0.02	299	2	0.195	0.006
BWC-3	0.02951	0.00008	9.83	0.01	299	1	0.187	0.006
TRTP	0.02959	0.00010	9.85	0.02	300	1	0.181	0.006
Cane Creek	0.03826	0.00007	9.62	0.02	1110	10	0.224	0.010
<b>Gas Phase</b>								
AM-75	0.03018	0.00005	10.1	0.02	304	2	0.191	0.006
AM-62	0.03032	0.00003	10.1	0.02	328	2	0.191	0.006
AM-11-E34	0.03099	0.00002	10.2	0.02	446	4	0.191	0.008
MM 31-42	0.03378	0.00006	10.1	0.05	819	28	0.189	0.006
MM 31-42 (dup)								
BI 24-31	0.03519	0.00031			505	4	0.281	0.001
BI 24-32 (dup)								
BH 10-31	0.03029	0.00007	10.1	0.02	295	2	0.191	0.006
HC 31-31	0.03029	0.00009	10.2	0.02	308	2	0.191	0.006
FF-2-19	0.03179	0.00002	10.2	0.02	678	6	0.193	0.009
FF-2-19 (dup)	0.03161	0.00005	10.2	0.02	634	4	0.203	0.005
Tohonalda 35-B	0.04127	0.00040	9.66	0.02	841	30	0.200	0.007
Tohonalda 1	0.04046	0.00008	9.68	0.06	888	16	0.221	0.022
Tohonalda 1 (dup)								
Anasazi 1			9.69	0.02	708	21	0.122	0.043
Sahgzie 1			9.69	0.02	573	12	0.177	0.024
Sahgzie 1 (dup)								
Monument-8N-2	0.03494	0.00002	10.0	0.02	525	11	0.139	0.015
Monument-8N-2 (dup)								
WM 22-43	0.03298	0.00004	9.80	0.03	395	4	0.198	0.011
WM 22-43 (dup)	0.03094	0.00005	9.80	0.03	356	3	0.190	0.008
WM 34-31	0.03209	0.00011			372	4	0.188	0.008
WM 34-31 (dup)	0.03200	0.00003	9.79	0.02	376	3	0.187	0.009
WM 34-33	0.03151	0.00004	9.82	0.03	346	4	0.186	0.010
McIntyre 17-21	0.08454	0.00018	8.80	0.01	3760	30	0.190	0.002
Lisbon D8-10					4530	150	0.141	0.010
Lisbon 10-33	0.06975	0.00009	8.99	0.03	3510	50	0.182	0.014
Lisbon 10-33 (dup)	0.06930	0.00011	9.01	0.04	3600	80	0.146	0.025
Lisbon B8-10	0.07181	0.00062	8.93	0.06	2620	30	0.171	0.007
Lisbon B8-10 (dup)					2710	20		

distribution throughout the basin (section 5.1 and 5.2). This gives a first order approximation of if there are any barriers to fluid flow in the basin. We use the fractionation in air derived noble gas ratios to estimate the extent of fluid interaction and migration, and correct noble gas concentrations (section 5.3). Finally, using this information, we develop a 1D vertical He diffusion model, to investigate diffusion barriers and flow through the stratigraphy (Section 5.4).

### 5.1. Assessing fluid provenance using noble gas isotope ratios

In order to investigate the distribution of noble gases across the basin, it is important to first understand their provenance. Terrestrial noble gas reservoirs (atmosphere, crust and mantle) have diagnostic isotopic compositions, meaning fluids sourced from each reservoir can be distinguished.

Helium isotopes in ASW are readily overprinted by the release of radiogenic  $^4\text{He}$  in the subsurface. The air-corrected  $^3\text{He}/^4\text{He}$

( $R_c/R_A$ ) is the sum of two components: the crust and the mantle. The helium isotope ratio associated with typical crustal radiogenic production is  $0.02R_A$  (Ballentine and Burnard, 2002) and sub-continental lithospheric mantle (SCLM) is  $6.1 \pm 2.1R_A$  (Day et al., 2015). Air corrected  $^3\text{He}/^4\text{He}$  values (0.005 to  $0.127R_A$ ) are consistent with significant radiogenic contributions (Fig. 3). The slightly elevated  $^3\text{He}/^4\text{He}$  (up to  $0.127R_A$ ) observed in the Navajo Aquifer to the southwest of the basin could either be a result of lower U and Th concentrations in the host rock, or the preferential migration of mantle derived He associated with mantle  $\text{CO}_2$  through the aquifer from the Monument Upwarp, as observed regionally and in other basinal systems (e.g., Crossey et al., 2016; Byrne et al., 2020). No  $\text{CO}_2$  concentrations were measured in the Navajo Aquifer, however where  $\text{CO}_2$  was measured we observe no relationship with helium (Supplementary Fig. 2), suggesting an absence of mantle  $\text{CO}_2$  in the basin interior. The primarily crustal signatures within these samples are in contrast to those measured

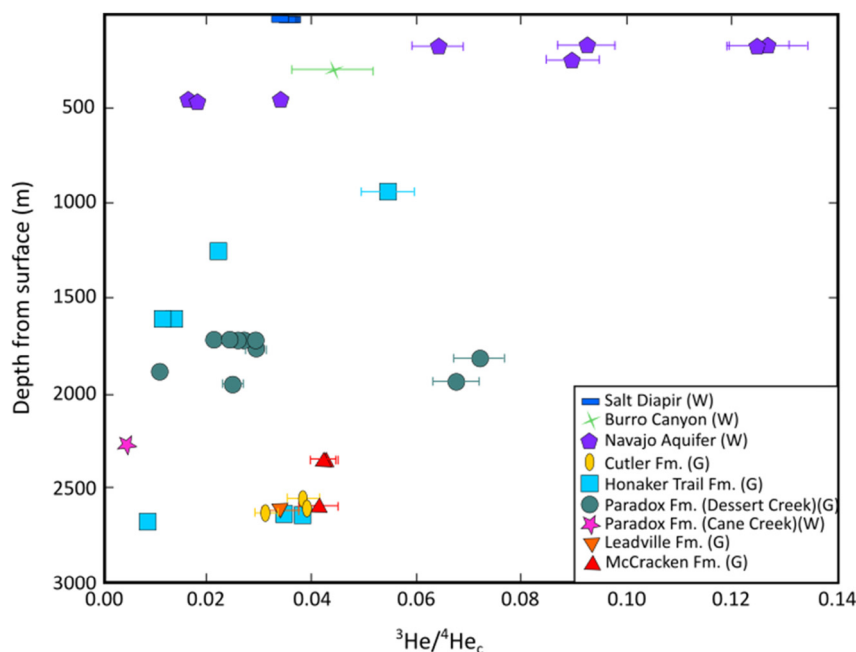


**Fig. 3.** Air Corrected  $^3\text{He}/^4\text{He}$  ( $R_c/R_a$ ) as a function of depth from the surface (m). G (gas) and W (water) represent the sample phase. Samples all have low  $^3\text{He}/^4\text{He}$  relative to sub continental lithospheric mantle (SCLM;  $6.1 \pm 2.1 R_a$ , Day et al., 2015) and are close to the typical radiogenic production value of  $0.02 R_a$  (Ballentine and Burnard, 2002). Elevated  $^3\text{He}/^4\text{He}$  in the Navajo aquifer are either the result of lower U and Th concentrations in the host rock, or the preferential migration of mantle derived He associated with mantle  $\text{CO}_2$  (e.g., Crossey et al., 2016; Byrne et al., 2020).

in distal  $\text{CO}_2$  fields ( $0.125\text{--}3.784 R_a$ ) which are mantle derived (Gilfillan et al., 2008).

Neon ( $^{21}\text{Ne}/^{22}\text{Ne}$ ,  $^{20}\text{Ne}/^{22}\text{Ne}$ ) and argon ( $^{40}\text{Ar}/^{36}\text{Ar}$ ) isotopes are consistent with mixing between atmospheric and radiogenic end-members (Fig. 4a). In the formations overlying the P.Fm, neon isotope ratios are air-like and deviations from the atmospheric value, in  $^{20}\text{Ne}/^{22}\text{Ne}$ , are consistent with mass fractionation effects (Fig. 4). However, significant deviations from the atmospheric Ne isotopic compositions are observed within and below the P.Fm that cannot be attributed to mass fractionation. Within the Desert Creek Member of the P.Fm, neon isotopes are consistent with radiogenic production within a high apparent oxygen/fluorine (O/F) environment (Lippmann-Pipke et al., 2011), whereas samples from the Cane Creek Member of the P.Fm, Leadville Fm and McCracken Fm plot closer to production from an environment with an average crustal O/F composition (Kennedy et al., 1990). The Leadville and McCracken Fms, have the most significant crustal Ne contributions and similar to values previously measured in the Leadville Fm at McElmo Dome in the southeast of the basin (Gilfillan et al., 2008).

Samples from the shallow Burro Canyon and Navajo aquifers have air-like  $^{40}\text{Ar}/^{36}\text{Ar}$  (298 to 300, where  $^{40}\text{Ar}/^{36}\text{Ar}_{\text{air}} = 298.6$ , Lee et al., 2006). The remaining samples have measurable  $^{40}\text{Ar}^*$  with elevated  $^{40}\text{Ar}/^{36}\text{Ar}$  signatures between 302 and 4,530. The  $^{40}\text{Ar}/^{36}\text{Ar}$  generally increases with increasing stratigraphic age and correlates with  $^{21}\text{Ne}$  excesses ( $^{21}\text{Ne}^*$ ) (Fig. 4, Table 2). The most significant  $^{40}\text{Ar}/^{36}\text{Ar}$  excesses (2,620–4,530) are found beneath the P.Fm in the Leadville and McCracken Fms.

Both Ne and Ar isotopes demonstrate a higher radiogenic isotopic contribution beneath the P.Fm compared to samples collected within and above it. We hypothesise from the noble gas isotope ratios that the P.Fm confining unit is acting as a near complete barrier to vertical gas diffusion within the basin, resulting in the accumulation of radiogenic noble gases beneath the P.Fm and the evolution of distinct fluid compositions above and below it. An exception to this is highly faulted regions in the Colorado Plateau, but outside our study area, which facilitate the upward migration of deep fluids (e.g., Crossey et al., 2006, 2016).

## 5.2. Radiogenic noble gases concentrations

In order to compare radiogenic noble gas ( $^4\text{He}$ ,  $^{21}\text{Ne}^*$  and  $^{40}\text{Ar}^*$ ) concentrations across the basin, measured hydrocarbon phase concentrations are used to calculate the initial noble gas concentration in the associated groundwater (e.g., Cheng et al., 2021; Byrne et al., 2020; Barry et al., 2018a, 2018b). Hydrocarbons are assumed to be initially devoid of all noble gases and inherit their atmospheric noble gas signature from solubility exchange with groundwater. The calculated concentrations of  $^{20}\text{Ne}$  and  $^{36}\text{Ar}$  in ASW are  $2.57 \times 10^{-7} \text{ cm}^3/\text{g}_{\text{water}}$  and  $1.65 \times 10^{-6} \text{ cm}^3/\text{g}_{\text{water}}$  respectively, based on assumed recharge conditions of  $10^\circ\text{C}$ , 0 M, 2000 m and a 10% Ne excess (Gilfillan et al., 2008). Noble gases will preferentially partition from the water phase into the gas/oil phase, due to relative solubilities, resulting in a systematically higher proportion of the less water-soluble noble gases in the gas/oil phase and a higher proportion of the more water-soluble noble gases remaining in the water phase (Kharaka and Specht, 1988; Fernández-Prini et al., 2003). The extent of this partitioning is moderated by volumes of water to oil/gas. Using the solubility-corrected noble gas ratios and concentrations of atmospheric noble gas in ASW, the concentration of radiogenic noble gases in the groundwater can be calculated from the sampled hydrocarbons (Table 3; SI.2). Concentrations of  $^4\text{He}$ ,  $^{21}\text{Ne}^*$  and  $^{40}\text{Ar}^*$  are correlated and are in agreement with typical crustal production ratios ( $^4\text{He}/^{40}\text{Ar}^* = 6.01$ ,  $^{21}\text{Ne}^*/^{40}\text{Ar}^* = 2.75 \times 10^{-7}$ ) (Supplementary Fig. 4; Ballentine and Burnard, 2002), however deviations to higher  $^{40}\text{Ar}^*$  are observed within the P.Fm due to its high  $^{40}\text{K}$  content (Hite, 1961).

Groundwater  $^4\text{He}$  concentration varies by 6 orders of magnitude from  $4.40 \times 10^{-8}$  to  $4.40 \times 10^{-2} \text{ cm}^3/\text{g}_{\text{water}}$ . While  $^4\text{He}$  concentrations are the lowest in the shallowest formations, there is no clear trend with depth below  $\sim 1000$  m (Fig. 5a). Salt tectonics have resulted in significant differences in formation thickness across the basin (i.e., Fig. 2) and therefore, we compare trends with depth by investigating the concentration vs. stratigraphic age (Fig. 5b). There is a clear increase in  $^4\text{He}$  concentrations with in-

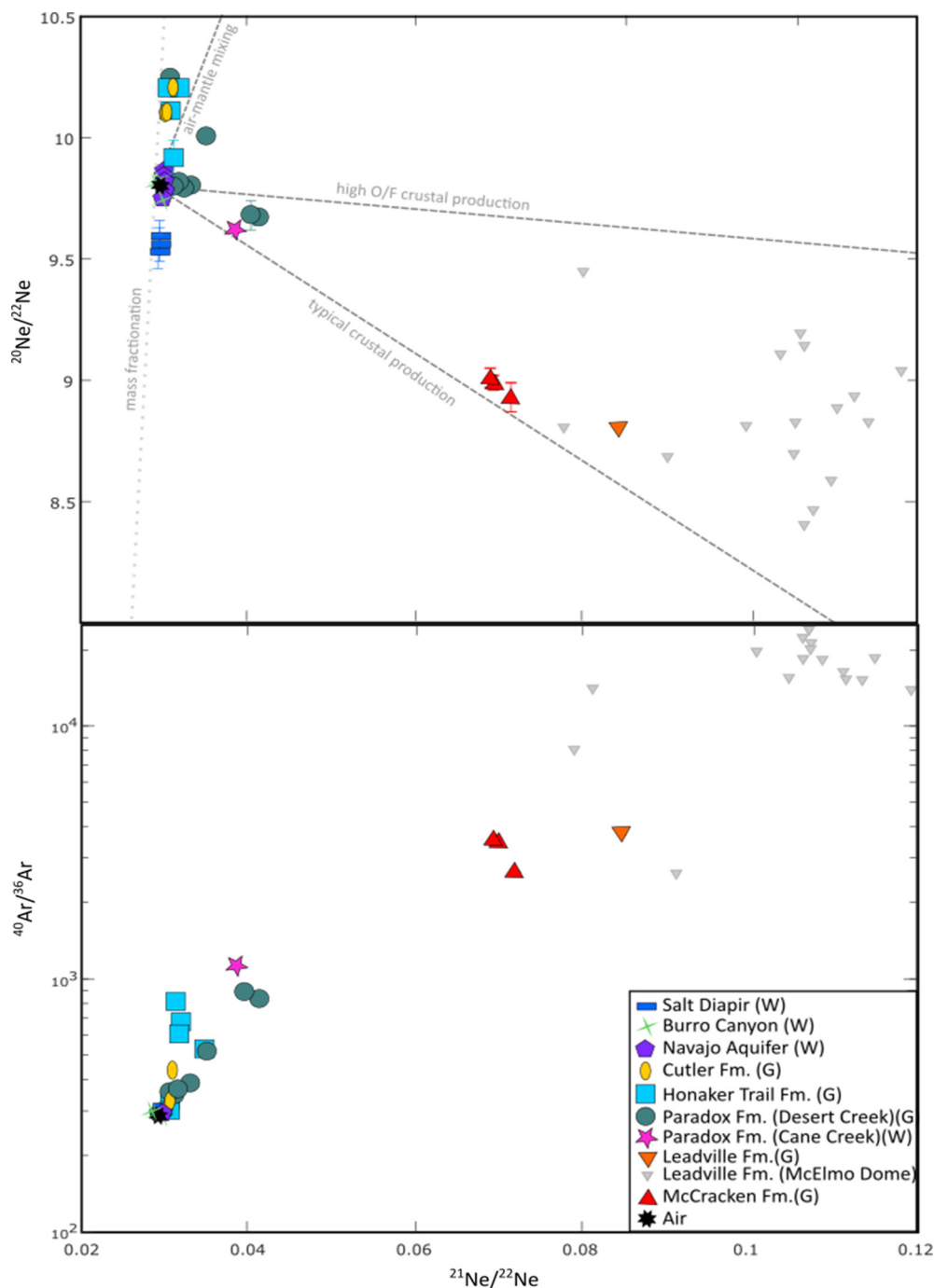


**Fig. 4.**  $^{21}\text{Ne}/^{22}\text{Ne}$  vs. a)  $^{20}\text{Ne}/^{22}\text{Ne}$  and b)  $^{40}\text{Ar}/^{36}\text{Ar}$  for all samples. G (gas) and W (water) represent the phase the sample was collected in. In the formations above the Paradox Formation (Burro Canyon, Navajo, Cutler and Honaker trail) radiogenic noble gases are largely air-like for neon or have relatively small radiogenic Ar excesses. In contrast, the Leadville and McCracken formations beneath the Paradox Formation contain significantly greater proportions of radiogenic noble gases and are consistent with those measured in McElmo Dome (Gilfillan et al., 2008), suggesting the two hydrological systems are disparate. Within the Paradox Formation, neon isotopes show evidence of both typical Oxygen/Fluorine (O/F) crust in the Cane Creek region and high O/F environments in the Desert Creek member.

creasing stratigraphic age. The lowest concentrations are in the shallow Burro Canyon Aquifer and the highest concentrations in the deepest McCracken Fm. Calculated in-situ  $^4\text{He}$  ages (1,750–3,790 Ma, Equation (1)) are significantly older than stratigraphic ages ( $\sim 359$ –382 Ma) below the P.Fm, suggesting an external  $^4\text{He}$  flux (Table 3). The shallow brines derived from dissolution of halite and gypsum in the Salt Diapir (P.Fm) are mostly meteoric and exhibits high sulfide concentrations (5.8–7.1 mmol/L) from bacterial sulphate reduction (Kim et al., 2022) which is being actively exsolved. Both gas stripping from  $\text{H}_2\text{S}$  formation and the meteoric

water content accounts for the lower measured  $^4\text{He}$  concentrations.

A similar trend is also observed in both  $^{40}\text{Ar}^*$  and  $^{21}\text{Ne}^*$ , with the highest concentrations in the basal Leadville and McCracken Fms below the P.Fm (Supplementary Fig. 4), consistent with the strongly nucleogenic  $^{21}\text{Ne}/^{22}\text{Ne}$  and radiogenic  $^{40}\text{Ar}/^{36}\text{Ar}$  ratios observed in these formations. To identify how the P.Fm is controlling the  $^4\text{He}$  distribution within the basin (Section 5.4), we first need to identify and quantify any fluid interaction (Section 5.3).



**Table 3**

Radiogenic noble gas concentrations in  $\text{cm}^3(\text{STP})/\text{g}_{\text{water}}$  within groundwater  $1\sigma$  errors. Concentrations in groundwater for the gas phase samples were calculating using the solubility corrected  $^4\text{He}/^{20}\text{Ne}_{(\text{sc})}$  (see supplementary information for details), measured  $^4\text{He}/^{20}\text{Ne}$  and solubility corrected  $^4\text{He}/^{36}\text{Ar}$  are also given.  $[^4\text{He}]_{\text{gw(c)}}$  is the  $^4\text{He}$  concentration in groundwater after correction for phase partitioning (cf. section 5.3).  $\wedge$  associated  $^4\text{He}$  residence times (in Ma) are calculated based on purely in-situ production (Eq. (1)).

Sample Name	$^4\text{He}_{\text{gw}}$ ( $\times 10^{-6}$ )	$\pm$	$^4\text{He age}^\wedge$ (Ma)	$\pm$	$^4\text{He}_{\text{gw(c)}}$ ( $\times 10^{-6}$ )	$\pm$	$^4\text{He age}_c^\wedge$ (Ma)	$\pm$	$^{21}\text{Ne}^*_{\text{gw}}$ ( $\times 10^{-12}$ )	$\pm$	$^{40}\text{Ar}^*_{\text{gw}}$ ( $\times 10^{-6}$ )	$\pm$	$^4\text{He}/^{20}\text{Ne}$	$\pm$	$^4\text{He}/^{20}\text{Ne}_{(\text{sc})}$	$\pm$	$^4\text{He}/^{36}\text{Ar}_{(\text{sc})}$	$\pm$
<b>Water phase (<math>\text{cm}^3(\text{STP})/\text{g}_{\text{water}}</math>)</b>																		
BOR 8E	1.13	0.03	0.11	0.05	11.6	0.6	0.55	0.28	1.71	0.07	7.36	0.35	80.2	3.9				
BOR 9E	1.14	0.03	0.11	0.06	11.3	0.5	0.54	0.27	1.80	0.07	9.27	0.44	78.3	3.8				
BOR 3E	1.55	0.05	0.15	0.075	11.8	0.6	0.56	0.28	2.17	0.09	6.28	0.30	81.3	3.9				
BOR 2E	1.86	0.06	0.18	0.09	11.3	0.5	0.54	0.27	1.71	0.07	5.38	0.25	77.9	3.8				
PW-4	0.044	0.001	0.037	0.007									0.315	0.012				
PW-4 (dup)	0.045	0.001	0.038	0.008									0.295	0.013				
PW-3	0.074	0.002	0.062	0.013									0.407	0.015				
PW-12	0.365	0.004	0.31	0.01									2.01	0.03				
PW-8																		
PW-8 (dup)	3.95	0.12	4.6	0.9									20.2	1.0				
PW-11	0.586	0.018	0.68	0.14									3.29	0.12				
PW-7	0.802	0.025	0.93	0.19									0.780	0.029				
STCEC	0.899	0.027	0.052	0.010									3.48	0.17				
BWC-1	0.759	0.023	0.044	0.009									2.79	0.10				
BWC-2	3.46	0.11	0.20	0.04									13.9	0.5				
BWC-3	8.26	0.25	0.47	0.09									34.4	1.7				
TRTP	18.5	0.6	1.1	0.2									82.6	4.1				
Cane Creek	213	2	10	5	6590	100	310	160	8.48	0.10	859	58	25600	400				
<b>Gas Phase (<math>\text{cm}^3(\text{STP})/\text{g}_{\text{water}}</math>)</b>																		
AM-75	33.5	4	5.2	1.0	33.8	3.8	5.3	1.1	3.85	0.02	8.64	0.15	130	7	130	7	98.4	3.6
AM-62	96.5	10.8	15	3	97.5	1.1	15	3	13.3	0.5	48.1	0.8	375	19	375	19	246	9
AM-11-E34	633	71	99	20	640	72	100	20	17.5	0.7	24	4	2460	126	2460	126	1720	63
MM 31-42	4140	540	213	43	4170	520	220	40	98.6	5.5	859	58	16200	1200	16100	1200	8950	780
BI 24-31	610	80	99	20					220	12			2390	170	2370	170	11600	900
BH 10-31	24.4	2.8	1.7	0.25	24.7	2.8	1.3	0.3	8.81	0.35			95.6	4.9	94.9	2.8	70.7	2.6
HC 31-31	67.7	7.6	3.5	0.7	68.4	7.7	3.5	0.7	3.43	0.14	15.5	0.3	265	14	263	14	151	5
FF-2-19	1310	150	677	13.5	1330	150	68	14	40.7	1.6	627	11	5140	260	5100	260	3350	120
FF-2-19 (dup)	1150	130	593	11.9	1160	130	60	12	37.6	1.4	554	19	4500	220	4470	220	3020	130
Tohonalda 35-B	12000	1800	426	213					6.54	0.13			35100	1300	46700	1800		
Tohonalda 1	8590	1290	305	152					177	7	973	23	25100	1300	33400	1700	6670	260
Anasazi 1	8800	1320	312	156							676	23	25700	1300	34200	1800	5540	260
Sahgzie 1	8710	1310	309	154							454	12	25400	1300	33800	1700	5000	200
Monument-8N-2	6000	900	213	106							374	10	17500	900	23300	1200	6040	250
WM 22-43	2720	410	96	48					58.8	2.4	159	3	1270	60	1690	80	1170	65
WM 34-31											122	2	6640	340	8830	450	1150	40
WM 34-31 (dup)	1940	290	68.8	34.4					44.4	1.8	129	2	5670	290	7540	390	1460	50
WM 34-33	1510	230	53.5	26.8					36.2	1.5	78.7	1.5	4410	230	5860	300	967	36
McIntyre 17-21	20300	2700	1750	350	20300	2700	1750	350	1710	110	5720	370	78800	6800	78800	6800	15800	1400
Lisbon D8-10											6980	470					74900	6400
Lisbon 10-33	44000	5000	3790	760	44100	5000	3800	800	1230	50	5300	110	171000	9000	171000	9000	33200	1200
Lisbon 10-33 (dup)	43700	4900	3760	750	43800	4900	3800	800	1220	50	5450	150	170000	9000	170000	9000	34000	1400
Lisbon B8-10	33400	4300	2880	580	33600	4340	2900	600	1310	70	3840	230	130000	9000	130000	9000	43500	3500

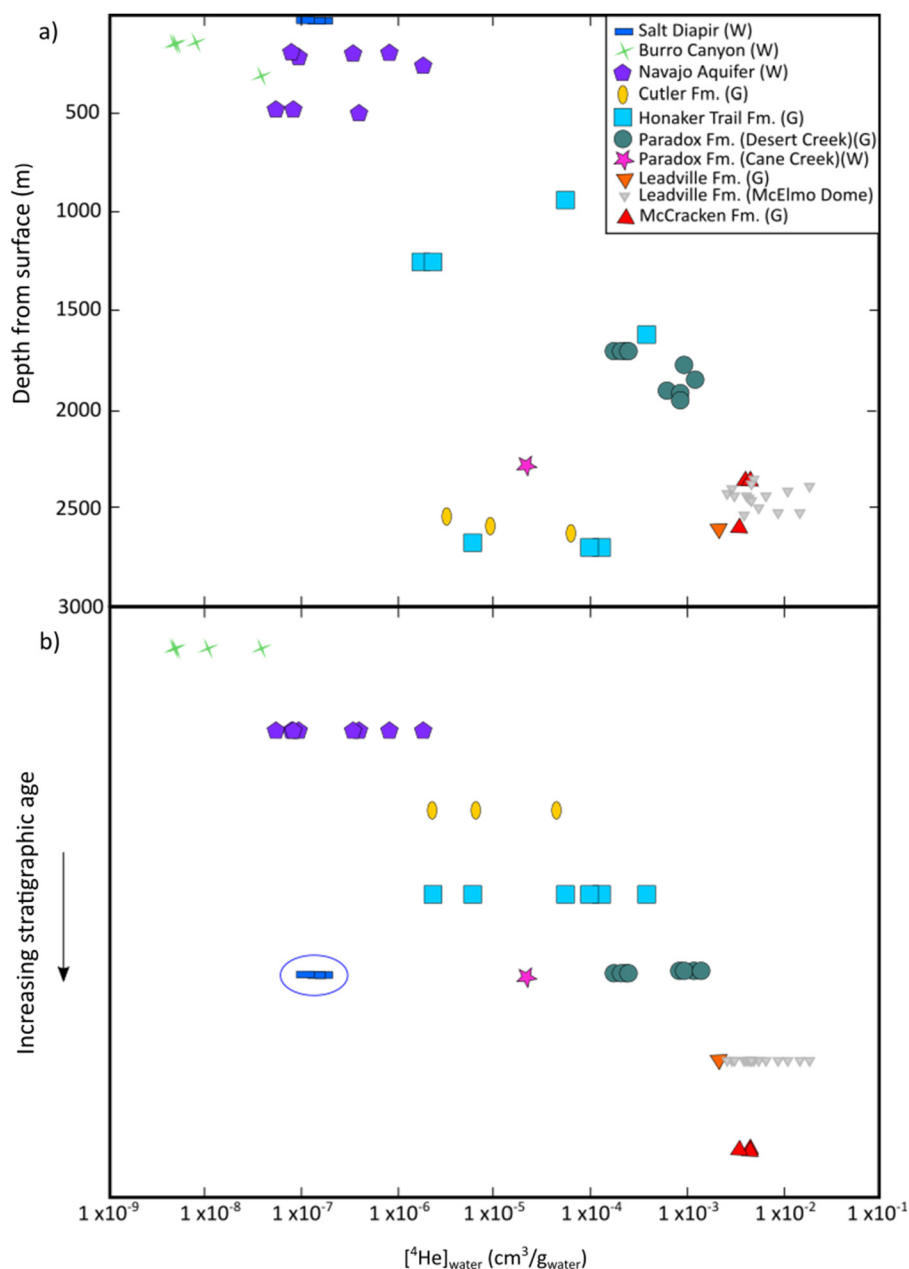


**Fig. 5.**  $^4\text{He}$  concentration in the water phase vs. a) depth and b) stratigraphic age. G (gas) and W (water) represent the phase the sample phase was collected in. 1 sigma errors are within symbol size. Samples show an increasing  $^4\text{He}$  concentration with depth/stratigraphic age. McElmo Dome samples are from Gilfillan et al. (2008). Salt Diapir samples (encircled on b) have lower concentrations than the rest of the Paradox Formation, likely due to their shallow, meteoric origin, gas exsolution and adjacent location next to the Dolores River.

### 5.3. Fractionation of the atmospheric noble gases

Understanding phase fractionation in a system is important for understanding the subsurface environment (e.g., fluid migration, relative volumes) and for correcting concentrations back to original source values. If a system is in equilibrium, the distribution of atmospheric noble gases ( $^{20}\text{Ne}$ ,  $^{36}\text{Ar}$ ,  $^{84}\text{Kr}$ ,  $^{130}\text{Xe}$ ) and ratios ( $^{20}\text{Ne}/^{36}\text{Ar}$ ,  $^{84}\text{Kr}/^{36}\text{Ar}$ ,  $^{130}\text{Xe}/^{36}\text{Ar}$ ) in each phase (e.g., water and gas, water and oil) can be predicted based on their relative solubility. Deviations from these predicted compositions are a result of phase fractionation (SI.4).

Groundwater samples from the Burro Canyon and Navajo aquifers, have  $^{20}\text{Ne}/^{36}\text{Ar}$  within error of ASW (Supplementary Table 2), suggesting little to no fluid interaction/phase fractionation has occurred. Similarly, we see  $^{20}\text{Ne}/^{36}\text{Ar}$  within oil-water equilib-

rium limits in the Desert Creek Member of the P.Fm hydrocarbon samples that were not subjected to enhanced oil recovery (EOR) techniques, indicating that they represent a closed system phase equilibrium between oil and water (Barry et al., 2018b; Tyne et al., 2021). Where water injection for EOR has occurred in the Desert Creek member (WM Field), samples have elevated  $^{20}\text{Ne}/^{36}\text{Ar}$ , as a result of air incorporation during EOR (Barry et al., 2018b; Tyne et al., 2021).

If groundwater contacts an undersaturated gas phase (e.g., a pocket of  $\text{CH}_4$ ), noble gases will partition into the gas phase (exsolution) resulting a decrease in  $^{20}\text{Ne}/^{36}\text{Ar}$  and increase in  $^{84}\text{Kr}/^{36}\text{Ar}$  (Barry et al., 2016).  $^{20}\text{Ne}/^{36}\text{Ar}$  below ASW (0.049 and 0.069) and  $^{84}\text{Kr}/^{36}\text{Ar}$  above ASW (0.0504–0.0621) are observed in the Salt Diapir (Supplementary Fig. 6a,b), consistent with exsolution alongside  $\text{H}_2\text{S}$  into the atmosphere. By modelling exsolution as an open

system, we find between 30–44% of the noble gases originally in the groundwater were stripped into a gas phase (Supplementary Fig. 6a,b, Supplementary Table 2). Following models by Barry et al. (2016) we predict the volume of gas required to exsolve relative to the water volume (G/W) for the Salt Diaper is between 0.028 and 0.042, suggesting that a larger volume of water, than exsolved gas, is required to explain the observed fractionation (SI.4). The groundwater  $^4\text{He}$  concentration ( $[^4\text{He}]_{\text{gwc}}$ ) can then be corrected for this gas loss using the solubility corrected  $^4\text{He}/^{20}\text{Ne}$  and  $^{20}\text{Ne}$  expected in ASW (Eq. (2)).

$$[^4\text{He}]_{\text{gwc}} = [^{20}\text{Ne}]_{\text{ASW}} \times ^4\text{He}/^{20}\text{Ne}_{\text{SC}} \quad (2)$$

where  $^4\text{He}/^{20}\text{Ne}_{\text{SC}}$  is the solubility corrected (for exsolution or partial redissolution) ratio (Table 3) and  $[^{20}\text{Ne}]_{\text{ASW}}$  is the expected concentration of  $^{20}\text{Ne}$  in ASW under recharge conditions (Supplementary Table 3).

Partial redissolution is a two-stage process. During the first stage, noble gases in groundwater are completely exsolved into a gas phase which was initially low in these elements. In the second stage, the noble gases in the gas phase redissolve into groundwater as a result of groundwater flow bringing gas stripped water into contact with the gas phase, or a change in the physical conditions (e.g., increase in pressure). Elevated  $^{20}\text{Ne}/^{36}\text{Ar}$  in the gas samples, in excess of that which can be explained by simple gas-water equilibrium, is observed both above (0.55–0.76, Cutler and Honaker Trail Fms) and below (0.19–0.34, Leadville and McCracken Fms) the P.Fm, consistent with partial redissolution (Supplementary Fig. 6c,d). Partial redissolution has previously been observed at McElmo Dome (Gilfillan et al., 2008). Groundwater flow through these units is in agreement with the relatively young (30–800 ka)  $^{81}\text{Kr}$  and  $^{14}\text{C}$  residence times (Kim et al., 2021, 2022; Noyes et al., 2021) and with the major ion and water stable isotope chemistry of the brines, which suggest there has been dissolution of the P.Fm evaporites as a result of influx of meteoric water (Kim et al., 2022). In the Cutler and Honaker Trail Fms (above the P.Fm), the proportion of noble gases that have been partially redissolved is between 87 and 96% (Eq. S9; Supplementary Table 2), which is significantly greater than the proportion redissolved in the Leadville and McCracken Fms (37–78%, Supplementary Fig. 6c,d) and suggests greater water-gas interaction in the Upper hydrostratigraphic unit. We also observe much greater water-to-gas (W/G) volumes in the Cutler and Honaker Trail Fms ( $W/G=38\text{--}49$ ) compared to below the P.Fm ( $W/G=7\text{--}24$ ) (Eq. S6–8; Supplementary Table 2), suggesting that the gas phases in the Cutler and Honaker Trail Fms have contacted a relatively greater volume of groundwater than in the Leadville and McCracken Fms below the P.Fm. The disconnect between the Upper and Lower hydrostratigraphic units suggests that lateral groundwater transport is more active above the P.Fm and that the P.Fm is a barrier between the two units, in agreement with the radiogenic isotope ratios (Section 5.1). The extent of partial redissolution can affect the  $^4\text{He}/^{20}\text{Ne}$  and therefore the calculated  $[^4\text{He}_{\text{gw}}]$  for the gas phase samples and any subsequent residence time estimates. By calculating the change in  $^4\text{He}/^{36}\text{Ar}$  and  $^{20}\text{Ne}/^{36}\text{Ar}$  with redissolution, we can predict the resulting change in  $^4\text{He}/^{20}\text{Ne}$ . We find that with 100% redissolution there is a 9.7% increase in the  $^4\text{He}/^{20}\text{Ne}$ . Below 95% redissolution, the effect of partial redissolution on the  $^4\text{He}/^{20}\text{Ne}$  is within error of our samples (<3%). Nevertheless, by quantifying the extent of partial redissolution, we can iteratively correct the  $^4\text{He}/^{20}\text{Ne}$  used for calculating  $[^4\text{He}_{\text{gwc}}]$  (Table 3).

These finding highlights the utility of stable noble gas isotopes in tracing and identifying the differences in hydrogeological regimes above and below an extensive salt unit, as well as quantifying horizontal fluid migration within a basin that needs to be considered when investigating the  $^4\text{He}$  distribution.

#### 5.4. Investigating $^4\text{He}$ distribution

Helium is the most sensitive noble gas to diffusion due to its high diffusivity in water (Jähne et al., 1987), making it an ideal tracer for investigating diffusional gas transport within a basin. To determine the role of the P.Fm in controlling fluid connectivity and compositions throughout the basin, we can compare the initial  $^4\text{He}$  distribution in groundwater (i.e., prior to any phase interactions), with predictions from a time-dependent vertical 1D  $^4\text{He}$  diffusion model (Cheng et al., 2021).

##### 5.4.1. Vertical 1D $^4\text{He}$ diffusion reference model

In our reference model we assume there are two sources of  $^4\text{He}$  within sedimentary units, one from in-situ radiogenic production and another from an external basement flux (Supplementary Fig. 7a). We also consider two mechanisms of  $^4\text{He}$  loss to a unit: meteoric recharge with ASW ('flushing') and diffusion to adjacent formations. We use the simplest scenario, of only in-situ production and vertical diffusion, to create a reference model that predicts the  $^4\text{He}$  concentrations expected in the groundwater (SI.5) (Cheng et al., 2021). Given the variable thicknesses of the sedimentary units across the basin, discrete models are presented for the different sampling areas. Assumptions about the parameters used in constructing these models (e.g., [U], [Th], porosity, age) are given in Supplementary Table 4. We assume the effective porosity in the P.Fm is approaching zero (0.00001%) (Beauheim and Roberts, 2002). Notably, U and Th concentrations within the P.Fm are poorly constrained (SI.3).

The  $^4\text{He}$  concentration in groundwater can then be predicted for the whole sedimentary column, assuming in-situ production and diffusion between lithological units (e.g., grey dashed line Fig. 6a,b, Eqs. S8–11, SI.5). Models predict that once the P.Fm has reached a thickness of  $\sim 50$  m,  $^4\text{He}$  concentrations become relatively constant, as diffusion is impeded and concentrations are dominated by in-situ production (Fig. 6, Supplementary Fig. 7b).

Within the Desert Creek Member of the P.Fm, samples can be split into two subgroups; those with lower  $^4\text{He}$  concentrations due to EOR in the WM Field ( $2.06 \pm 0.61 \times 10^{-3} \text{ cm}^3/\text{g}_{\text{water}}$ ) and those which have not been subject to EOR ( $8.82 \pm 2.13 \times 10^{-3} \text{ cm}^3/\text{g}_{\text{water}}$ ) (Fig. 6a). By comparing the  $^4\text{He}$  concentrations in the samples in the P.Fm which have not been subjected to EOR to the reference model, we observe that  $^4\text{He}$  concentrations are remarkably constant over the range of depths sampled and are consistent with those predicted for in-situ production alone. This agrees with the model and demonstrates that the P.Fm is in fact an effective seal, acting as a barrier to  $^4\text{He}$  diffusion and fluid communication, consistent with the observed noble gas elemental ratios. Although this result is not necessarily surprising, as salt is known to be an effective trap for hydrocarbon migration (e.g., Wescott and Hood, 1994), the verification that salt can act as a regional barrier to mobile elements such as  $^4\text{He}$ , could have implications for  $^4\text{He}$  and  $\text{H}_2$  accumulations and prospecting. In addition, there are significant considerations for crustal fluid dating, as the assumption of a constant external  $^4\text{He}$  flux throughout the stratigraphy, used in residence times calculations, is not valid where salt formations are prohibiting diffusion.

$^4\text{He}$  concentrations in the samples both above and below the P.Fm are not consistent with the reference model (Fig. 6a,b). Deviations from the reference models can provide insights into the rates and timings of additional processes (e.g., groundwater circulation, basement flux) occurring within the basin, and allow us to investigate cross formational gas migration.

##### 5.4.2. Identification of lateral advective flow

Samples taken from above the P.Fm (Burro Canyon and Navajo aquifers and the Cutler and Honaker Trail Fms) have  $^4\text{He}$  concen-

trations lower than predicted by our reference model (grey dashed line; Fig. 6). One mechanism that can lower the  $^4\text{He}$  concentrations is lateral (advective) flow of meteoric water into a unit. This meteoric 'flushing' through a stratigraphic unit decreases the  $^4\text{He}$  concentration. We can simulate this as 'on-off' system within the diffusive model: During complete flushing, the  $^4\text{He}$  concentration is effectively 'reset' to ASW concentrations and once lateral flow ceases,  $^4\text{He}$  accumulation is restarted. Complete flushing of meteoric water has been added to the  $^4\text{He}$  diffusional model from the recent denudation of the Colorado Plateau ( $\sim 6\text{Ma}$ ; Lazear et al., 2011; Karlstrom et al., 2012; Murray et al., 2019) to 5 ka in the Burro Canyon Aquifer, to 25 ka in the Navajo Aquifer (average  $^{14}\text{C}$  groundwater residence time; Noyes et al., 2021), and to  $\sim 0.5\text{ Ma}$  in the Cutler and Honker Trail Fms based on preliminary  $^{81}\text{Kr}$  results (Kim et al., 2021, 2022) (Fig. 6c,d). Meteoric recharge in these units accounts for the lower  $^4\text{He}$  concentrations observed within the samples overlying the P.Fm (Fig. 6c,d). This is in agreement with the fractionation observed in atmospheric noble gas ratios (Section 5.3), major ion and isotopic composition of the brines (Kim et al., 2022), and radiocarbon ages (Noyes et al., 2021).

Several samples (PW4, PW8, BWC2, BWC3, TRTP) have higher concentrations than predicted by the model, this deviation could result from the variation in groundwater residence time (e.g., 3.3–11 ka in the Burro Canyon Aquifer, Noyes et al., 2021), meaning  $^4\text{He}$  concentrations in the model are underestimated, from upwelling of deeper fluid through faults or from differences in U and Th concentrations of aquifer minerals.

Despite having  $^4\text{He}$  concentrations greater than can be explained by in-situ production (Fig. 6b), the fractionation in the atmospheric noble gas ratios (Section 5.3),  $^{81}\text{Kr}$  residence time ( $\sim 0.8\text{ Ma}$ ), water isotopes and major ion composition of the brines suggest that there has also been some meteoric water influx below the P.Fm (Kim et al., 2021, 2022). PHREEQC inverse modelling suggests that 95.8% of the groundwater in the Leadville Limestone is meteoric while 4.2% is remaining paleo-evaporated seawater-derived brines (Kim et al., 2022). Therefore, we also model meteoric flushing from 6 – 0.8 Ma in the Pinkerton, Molas, Leadville, Ouray and McCracken Fms beneath the P.Fm but include incomplete flushing with 4.2% 'old'  $^4\text{He}$  rich groundwaters remaining.

#### 5.4.3. Determining the basement helium flux

Regardless of whether there is meteoric flushing below the P.Fm,  $^4\text{He}$  concentrations in the Leadville and McCracken Fms are higher than can be explained solely by in-situ production and a basement flux of  $^4\text{He}$  is required (grey dashed reference line and blue line Fig. 6b,d). A volatile flux from the Precambrian basement is in agreement with previous observations of radiogenic Sr in the brines below the P.Fm (Crossey et al., 2006, 2016; Kim et al., 2022). Assuming lateral flow through these units from 6–0.8 Ma (approximate  $^{81}\text{Kr}$  residence time, Kim et al., 2020, 2021) and incomplete flushing with 4.2% 'old' water (enriched in  $^4\text{He}$ ) remaining (Kim et al., 2022), we find a constant basement flux of between  $14.5 - 70 \times 10^{-6} \text{ mol } ^4\text{He}/\text{m}^2/\text{yr}$  (purple and orange lines respectively, Fig. 6d) is required to fit the model to the measured  $^4\text{He}$  concentrations in these units. This is significantly greater than the average basement flux ( $1.47 \times 10^{-6} \text{ mol } ^4\text{He}/\text{m}^2/\text{yr}$ , yellow line Fig. 6d; Torgersen and Clarke, 1985).

Elevated  $^4\text{He}$  fluxes similar to that predicted by the model are observed in volcanic areas and areas under tectonic strain (Torgersen, 2010). However, the intrusion of the proximal La Sal mountains occurred approximately 20 – 31 Ma (Rønnevik et al., 2017), and the associated heat pulse is thought to be short-lived (Getz, 2020). Alternatively, if a larger portion of fluid enriched in  $^4\text{He}$  is trapped during flushing, a smaller basement flux will be required. It is important to note here that none of these scenarios are mutually exclusive and a combination of them is possible. Additionally,

if flushing of these units ended prior to 0.8 Ma, a lower basement flux would fit the model; however even with no flushing, a basement flux is still required. A basement  $^4\text{He}$  flux combined with P.Fm diffusional barrier indicates that He could accumulate beneath the salt.

## 6. Summary and conclusions

We present noble gas isotope and abundance data from 36 different samples collected in the Paradox Basin. These samples range across 7 stratigraphic units (Cretaceous–Devonian) and include a thick evaporite unit (Pennsylvanian Paradox Formation, P.Fm). By sampling fluids across a range of stratigraphic units we were able to investigate fluid communication above and below a regional salt layer and between different hydrostratigraphic units within a heterogeneous basin.

Low  $^3\text{He}/^4\text{He}$  measured across all units is consistent with the noble gases in the system being predominantly groundwater-derived, with radiogenic overprinting. Radiogenic noble gas concentrations ( $^4\text{He}$ ,  $^{21}\text{Ne}^*$  and  $^{40}\text{Ar}^*$ ) and isotope ratios ( $^{40}\text{Ar}/^{36}\text{Ar}$  and  $^{21}\text{Ne}/^{22}\text{Ne}$ ) increase with depth, consistent with increased accumulation of isotopes formed by crustal production with time, however there is a significant difference in the ratios above and below of the P.Fm as a result of P.Fm acting as a barrier to gas diffusion.

We show that deviations from ASW in atmosphere-derived noble gas ratio ( $^{20}\text{Ne}/^{36}\text{Ar}$ ,  $^{84}\text{Kr}/^{36}\text{Ar}$  and  $^{130}\text{Xe}/^{36}\text{Ar}$ ) are a result of phase partitioning during fluid interactions. There is evidence of partial meteoric flushing of remnant basinal brines both below and above the P.Fm, in agreement with the major ion composition of the brines and  $^{81}\text{Kr}$  ages (Kim et al., 2021, 2022). Furthermore, we observe greater fluid phase interactions in the samples taken above the P.Fm than below suggesting that the hydrostratigraphic units above and below the P.Fm are independent, with the upper hydrological regime being more mobile.

Considering both in-situ radiogenic production and external helium basement fluxes, we develop vertical 1D  $^4\text{He}$  diffusion model. We find that the P.Fm is impermeable to  $^4\text{He}$  diffusion, allowing for the accumulation of  $^4\text{He}$  and radiogenic noble gases below. The verification that evaporites are regionally impermeable to diffusion, of even the most volatile elements, is important for sub-salt helium and hydrogen exploration and storage. Deviations from the theoretically calculated  $^4\text{He}$  diffusion reference model can largely be accounted for by meteoric water recharge, seen in the atmospheric noble gas ratios and likely associated with the recent denudation of the Colorado Plateau. High helium concentrations observed beneath the P.Fm are likely a result of a  $^4\text{He}$  basement flux and best explained combined with only partial flushing of the units. Typically, the determination of groundwater residence time assumes a simple system of in-situ production and a potential diffusive external flux from below, usually based on an assumed average crustal porosity (Torgersen and Clarke, 1985; Zhou and Ballentine, 2006). Through the development of the  $^4\text{He}$  diffusional models (e.g. Cheng et al., 2021), we show that the magnitude of the basement flux and lithology type can control the diffusive helium flux. For example, below the P.Fm, where there is a high basement  $^4\text{He}$  flux and diffusion into shallow formations is inhibited,  $^4\text{He}$  can accumulate and the  $^4\text{He}$  residence time would be overestimated. Whereas above the P.Fm, fluid circulation and lack of diffusion from the deepest formations would lead to an underestimation of  $^4\text{He}$  residence times. Therefore, an understanding and consideration of the basin architecture and history is critical to accurately determine  $^4\text{He}$  groundwater residence times.

We show that using the stable noble gas isotopes and extent of fluid migration in the basin, the dichotomous hydrostratigraphic units can be identified and the efficacy of the reservoir seal (i.e.,

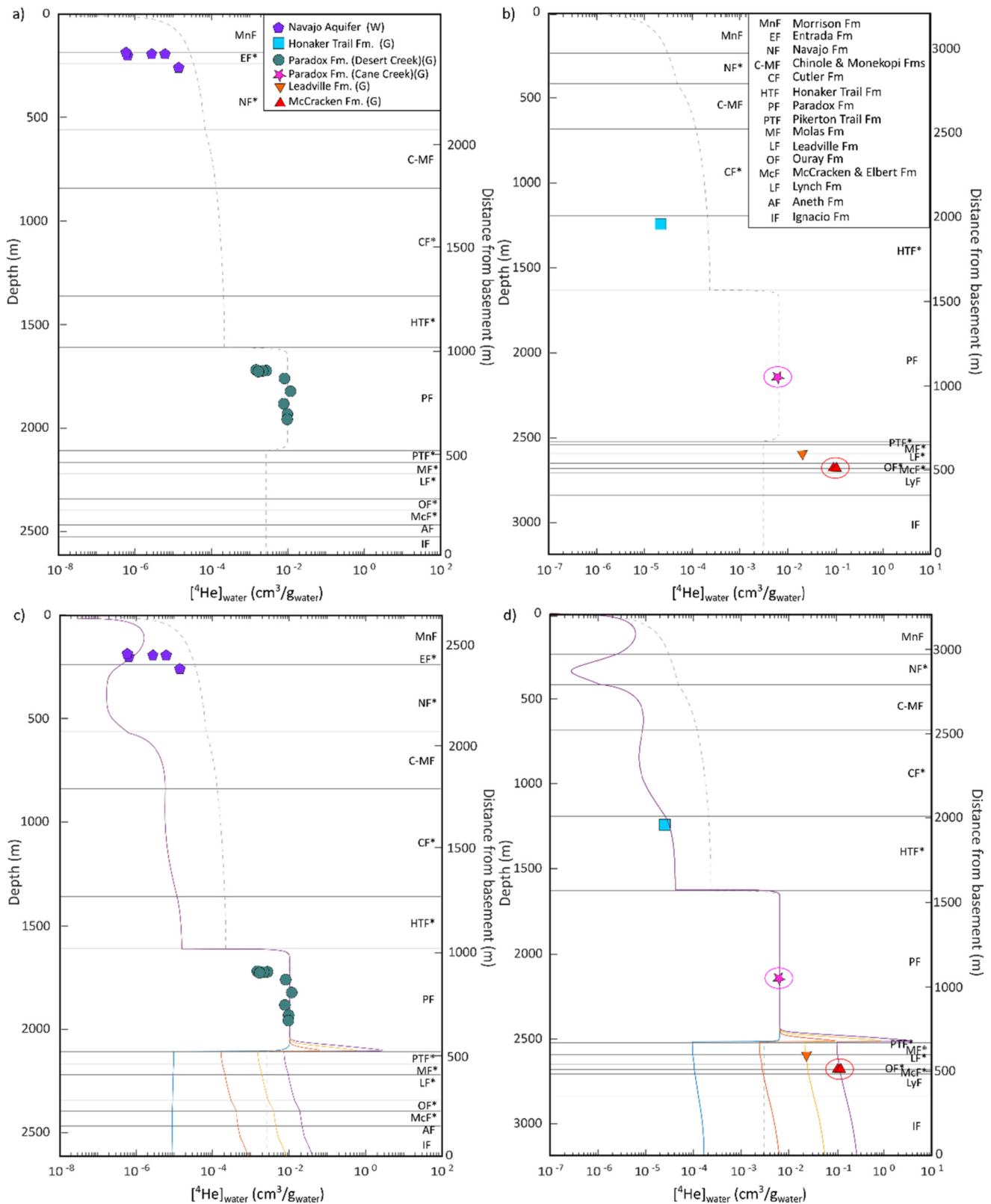


**Fig. 6.** Vertical 1D diffusion model  $^4\text{He}$  profiles compared with water concentrations inferred for the samples for a) Greater Aneth Oil Field, b) Lisbon Southeast Gas Field, as a function of depth and distance from the Precambrian basement. 1 sigma errors are within symbol size. a) and b) represent the 'reference' model for  $^4\text{He}$  concentrations in groundwater i.e., in-situ helium production, zero basement flux, no horizontal flow (grey dashed line). McCracken and Paradox (Cane Creek) formations (encircled on b,d) have been transposed from their own discrete models to the appropriate depth and concentration onto profile b/d.  $^4\text{He}$  diffusion is limited to the bottom ~50 m of the Paradox Formation (P.Fm) and the P.Fm samples can be explained solely by in-situ production. Concentrations lower than predicted by the reference model suggest lateral flushing through these units, where  $^4\text{He}$  concentrations greater than predicted require a  $^4\text{He}$  basement flux. c) and d) represent the modelled  $^4\text{He}$  concentration profiles or groundwater with lateral flow (flushed units marked with \*) for different basement fluxes. Modelled basement fluxes (in  $\text{mol}/\text{m}^2/\text{yr}$ ) are as follows: blue=0; yellow= $1.5 \times 10^{-6}$  (crustal average; Torgersen and Clarke, 1985); purple= $14.5 \times 10^{-6}$  (required to fit the Leadville Formation sample in the Lisbon Southeast Field); and orange= $70 \times 10^{-6}$  (required to fit McCracken samples within the Lisbon Field). The convergence of modelled flux lines in the P.Fm is a result of no diffusion within the formation and demonstrates that the P.Fm is effective at preventing vertical communication to the shallower formations.



P.Fm) can be quantified. This is critical in understanding subterranean modern and paleo-fluid flow within sedimentary basins, such as in the Paradox Basin, as well as for dating crustal fluids. Stratigraphy and regional faulting ultimately controls the connectivity and hydrogeology of various sedimentary reservoirs and understanding the nature and extent of communication between different fluid reservoirs is critical for resource exploration and storage of alternative energy and anthropogenic waste within the subsurface.

### CRediT authorship contribution statement

The project was conceived by RLT, JCM and CJB. RLT performed the noble gas isotopic analysis, with help of DJH, managed the project and prepared the first draft of the manuscript. RLT, JHK and JCM collected the samples. Noble gas modelling was developed by RLT, PHB, AC and CJB. All authors contributed to the final manuscript.

### Declaration of competing interest

The authors declare that they have no known competing financial interests or personal relationships that could have appeared to influence the work reported in this paper.

### Acknowledgements

This work was supported by a Natural Environment Research Council studentship to R.L. Tyne (Grant ref. NE/L002612/1). We gratefully acknowledge the William F. Keck Foundation for support of this research, and the National Science Foundation (NSF EAR #2120733). J.C. McIntosh and C.J. Ballentine are fellows of the CIFAR Earth4D Subsurface Science and Exploration Program. The authors would like to acknowledge the U.S. Bureau of Reclamation, Paradox Resources, Navajo Petroleum, US Oil and Gas INC, Anson Resources, Lantz Indergard (Lisbon Valley Mining Co.), Ambria Dell'Oro and Mohammad Marza for help with sampling. We also thank David J. Byrne and R  ta Karolyt   for their helpful comments on an earlier version of the manuscript, and Grant Ferguson for helpful discussions on Paradox Basin hydrogeology.

### Appendix A. Supplementary material

Supplementary material related to this article can be found online at <https://doi.org/10.1016/j.epsl.2022.117580>.

### References

- Baars, D.L., Stevenson, G.M., 1982. Subtle Stratigraphic Traps in Paleozoic Rocks of Paradox Basin. In: Halbouty, M.T. (Ed.), *The Deliberate search for the subtle trap*. AAPG Special Volume, pp. 131–158.
- Baars, D.L., 1996. Pre-Pennsylvanian Paleotectonics—Key to Basin Evolution and Petroleum Occurrences in Paradox Basin, Utah and Colorado. *Am. Assoc. Pet. Geol. Bull.* 50.
- Ballentine, C.J., Burgess, R., Marty, B., 2002. Tracing fluid origin, transport and interaction in the crust. In: Porcelli, D., Ballentine, C.J., Wieler, R. (Eds.), *Noble Gases in Geochemistry and Cosmochemistry*. In: *Reviews in Mineralogy and Geochemistry*, vol. 47. Geochemical Society, Mineralogical Society of America, pp. 539–614. Chapter 13.
- Ballentine, C.J., Burnard, P.G., 2002. Production, release and transport of noble gases in the continental crust. In: Porcelli, D., Ballentine, C.J., Wieler, R. (Eds.), *Noble Gases in Geochemistry and Cosmochemistry*. In: *Reviews in Mineralogy and Geochemistry*, vol. 47. Geochemical Society, Mineralogical Society of America, pp. 481–538. Chapter 12.
- Ballentine, C.J., O'Nions, R.K., Oxburgh, E.R., Horvath, F., Deak, J., 1991. Rare gas constraints on hydrocarbon accumulation, crustal degassing and groundwater flow in the Pannonian Basin. *Earth Planet. Sci. Lett.* 105, 229–246.
- Barbeau, D.L., 2003. A flexural model for the Paradox Basin: implications for the tectonics of the Ancestral Rocky Mountains: A flexural model for the Paradox Basin. *Basin Res.* 15, 97–115.
- Barry, P.H., Lawson, M., Meurer, W.P., Cheng, A., Ballentine, C.J., 2018a. Noble gases in deepwater oils of the U.S. Gulf of Mexico. *Geochim. Geophys. Geosyst.* 19, 4218–4235.
- Barry, P.H., Kulongoski, J.T., Tyne, R.L., Landon, M.K., Gillespie, J.M., Stephens, M.J., Hillegonds, D.J., Byrne, D.J., Ballentine, C.J., 2018b. Tracing enhanced oil recovery signatures in casing gases from the Lost Hills oil field using noble gases. *Earth Planet. Sci. Lett.* 496, 57–67.
- Barry, P.H., Lawson, M., Meurer, W.P., Warr, O., Mabry, J.C., Byrne, D.J., Ballentine, C.J., 2016. Noble gases solubility models of hydrocarbon charge mechanism in the Sleipner Vest gas field. *Geochim. Cosmochim. Acta* 194, 291–309.
- Beitler, B., Chan, M.A., Parry, W.T., 2003. Bleaching of Jurassic Navajo Sandstone on Colorado Plateau Laramide highs: Evidence of exhumed hydrocarbon supergiants? *Geology* 31 (12), 1041–1044.
- Beauheim, R.L., Roberts, R.M., 2002. Hydrology and hydraulic properties of a bedded evaporite formation. *J. Hydrol.* 259 (1–4), 66–88.
- Bremkamp, W., Harr, C.L., 1988. Area of least resistance to fluid movement and pressure rise: Paradox Valley Unit, Salt Brine Injection Project, Bedrock, Colorado: a report prepared for the U.S. Bureau of Reclamation, Denver, Colorado, p. 39.
- Byrne, D.J., Barry, P.H., Lawson, M., Ballentine, C.J., 2020. The use of noble gas isotopes to constrain subsurface fluid flow and hydrocarbon migration in the East Texas Basin. *Geochim. Cosmochim. Acta* 268, 186–208.
- Cheng, A., Sherwood Lollar, B., Warr, O., Ferguson, G., Idiz, E., Mundle, S.O.C., Barry, P.H., Byrne, D., Mabry, J., Ballentine, C.J., 2021. Determining the role of diffusion and basement flux in controlling <sup>4</sup>He distribution in sedimentary basin fluids. *Earth Planet. Sci. Lett.* 574, 117175.
- Craddock, W.H., Blondes, M.S., DeVera, C.A., Hunt, A.G., 2017. Mantle and crustal gases of the Colorado Plateau: Geochemistry, sources, and migration pathways. *Geochim. Cosmochim. Acta* 213, 346–374.
- Craig, H., Lupton, J.E., 1976. Primordial neon, helium, and hydrogen in oceanic basalts. *Earth Planet. Sci. Lett.* 31, 369–385.
- Crossey, L.J., Fischer, T.P., Patchett, P.J., Karlstrom, K.E., Hilton, D.R., Newell, D.L., Huntoon, P., Reynolds, A.C., de Leeuw, G.A.M., 2006. Dissected hydrologic system at the Grand Canyon: Interaction between deeply derived fluids and plateau aquifer waters in modern springs and travertine. *Geology* 34, 25–28.
- Crossey, L.J., Karlstrom, K.E., Springer, A.E., Newell, D., Hilton, D.R., Fischer, T., 2009. Degassing of mantle-derived CO<sub>2</sub> and He from springs in the southern Colorado Plateau region—Neotectonic connections and implications for groundwater systems. *Geol. Soc. Am. Bull.* 121 (7–8), 1034–1053.
- Crossey, L.J., Karlstrom, K.E., Schmandt, B., Crow, R., Colman, D., Cron, B., Takacs-Vesbach, T.D., Dahm, C., Northrup, D.E., Hilton, D.R., Ricketts, J.R., Lowry, A.R., 2016. Continental smokers couple mantle degassing and unique microbiology within continents. *Earth Planet. Sci. Lett.* 435, 22–30.
- Day, J.M., Barry, P.H., Hilton, D.R., Burgess, R., Pearson, D.G., Taylor, L.A., 2015. The helium flux from the continents and ubiquity of low-<sup>3</sup>He/<sup>4</sup>He recycled crust and lithosphere. *Geochim. Cosmochim. Acta* 153, 116–133.
- Dockrill, B., Shipton, Z.K., 2010. Structural controls on leakage from a natural CO<sub>2</sub> geologic storage site: Central Utah, U.S.A. *J. Struct. Geol.* 32 (11), 1768–1782.
- Ferguson, F., McIntosh, J.C., Grasby, S.E., Hendry, M.J., Jasechko, A., Lindsay, M.B., Luijendijk, E., 2018. The persistence of Brines in Sedimentary Basins. *Geophys. Res. Lett.* 45, 4851–4858.
- Fern  ndez-Prini, R., Alvarez, J.L., Harvey, A.H., 2003. Henry's Constants and Vapor-Liquid Distribution Constants for Gaseous Solutes in H<sub>2</sub>O and D<sub>2</sub>O at High Temperatures. *J. Phys. Chem. Ref. Data* 32, 903–916.
- Getz, C.M., 2020. Igneous-related hydrothermal systems in a saline basinal setting: La Sal Mountains, Paradox Basin, Utah. Masters Thesis. University of Arizona.
- Gillfillan, S.M.V., Ballentine, C.J., Holland, G., Blagburn, D., Lollar, B.S., Stevens, S., Schoell, M., Cassidy, M., 2008. The noble gas geochemistry of natural CO<sub>2</sub> gas reservoirs from the Colorado Plateau and Rocky Mountain provinces, USA. *Geochim. Cosmochim. Acta* 72, 1174–1198.
- Hanshaw, B.B., Hill, G.A., 1969. Geochemistry and hydrodynamics of the Paradox Basin region, Utah, Colorado and New Mexico. *Chem. Geol.* 4, 263–294.
- Harr, C.L., 1996. Paradox Oil and Gas Potential of the Ute Mountain Ute Indian Reservation: Phase II Geology/Seismic Study. *Geology and Resources of the Paradox Basin*. Utah Geological Association, pp. 13–28.
- Hendry, M.J., Kotzer, T.G., Solomon, D.K., 2005. Sources of radiogenic helium in clay till aquitard and its use to evaluate the timing of geologic events. *Geochim. Cosmochim. Acta* 65 (2), 475–483.
- Hilton, D.R., 1996. The helium and carbon isotope systematics of a continental geothermal system: results from monitoring studies at Long Valley caldera (California, USA). *Chem. Geol.* 127.
- Hite, R.J., 1961. Potash-bearing evaporite cycles in the salt anticlines of the Paradox basin, Colorado and Utah, in Short papers in the geologic and hydrogeologic sciences: U.S. Geological Survey Professional Paper 424D, pp. D135–D138.
- Hite, R.J., Buckner, D.H., 1981. Stratigraphic Correlations, Facies Concepts, and Cyclicity in Pennsylvanian Rocks of the Paradox Basin. In: *Geology of the Paradox Basin*. Rocky Mountain Association of Geologists 1981 Field Conference.
- J  hne, B., Heinz, G., Dietrich, W., 1987. Measurement of the diffusion coefficients of sparingly soluble gases in water. *J. Geophys. Res., Oceans* 92, 10767–10776.
- Karlstrom, K.E., Coblenz, D., Dueker, K., Ouimet, W., Kirby, E., Van Wijk, J., Schmandt, B., Kelley, S., Lazear, G., Crossey, L.J., Crow, R., Aslan, A., Darling, A.,

- Aster, R., McCarthy, J., Hanse, S.M., 2012. Mantle-driven dynamic uplift of the Rocky Mountains and Colorado Plateau and its surface response: Toward a unified hypothesis. *Lithosphere* 4 (1), 3–22.
- Kennedy, B.M., Hiyagon, H., Reynolds, J.H., 1990. Crustal neon: a striking uniformity. *Earth Planet. Sci. Lett.* 98, 277–286.
- Kharaka, Y.K., Specht, D.J., 1988. The solubility of noble gases in crude oil at 25–100 °C. *Appl. Geochem.* 3, 137–144.
- Kim, J.-H., Bailey, L., Noyes, C., Tyne, R.L., Ballentine, C.J., Person, M., Ma, L., Barton, M.D., Barton, I.F., Reiners, P., Ferguson, G., McIntosh, J.C., 2022. Hydrogeochemical evolution of formation waters responsible for sandstone bleaching and ore mineralization in the Paradox Basin. *Geol. Soc. Am. Bull.* <https://doi.org/10.1130/B36078.1>.
- Kim, J.-H., Ferguson, G.A.G., Person, M.A., Jiang, W., Lu, Z.-T., Yang, G.-M., Tyne, R.L., Ballentine, C.J., Reiners, P., McIntosh, J.C., 2021. Krypton Isotopes Constrain Timing of Regional Meteoric Circulation Enhanced by Rapid Denudation. In: AGU Abstracts. AGU, New Orleans, LA and Online.
- King, V.M., Block, L.V., Yeck, W.L., Wood, C.K., Derouin, S.A., 2014. Geological structure of the Paradox Valley Region, Colorado, and relationship to seismicity induced by deep well injection. *J. Geophys. Res., Solid Earth* 119, 4955–4978.
- Lazear, G.D., Karlstrom, K.E., Aslan, A., Schmandt, B., Beard, L.S., CREST Working Group, 2011. Denudational flexural isostasy of the Colorado Plateau: Implications for incision rates and tectonic uplift. In: Beard, L.S., Karlstrom, K.E., Young, R.A., Billingsley, G.H. (Eds.), *C Revolution 2—Origin and Evolution of the Colorado River System*, Workshop Abstracts: U.S. Geological Survey Open-File Report 2011-1210, pp. 287–295.
- Lee, J.-Y., Marti, K., Severinghaus, J.P., Kawamura, K., Yoo, H.-S., Lee, J.B., Kim, J.S., 2006. A re-determination of the isotopic abundances of atmospheric Ar. *Geochim. Cosmochim. Acta* 70, 4507–4512.
- Lippmann-Pipke, J., Sherwood Lollar, B., Niedermann, S., Stronick, N.A., Naumann, R., van Heerden, E., Onsott, T., 2011. Neon identifies two billion year old fluid component in Kaapvaal Craton. *Chem. Geol.* 283, 287–296. <https://doi.org/10.1016/j.chemgeo.2011.01.028>.
- Masbruch, M., Gardner, P.M., Nelson, N.C., Heilweil, V.M., Solder, J.E., Hess, M.D., McKinney, T.S., Briggs, M.A., Solomon, D.K., 2019. Evaluation of Groundwater Resources in the Spanish Valley Watershed, Grand and San Juan Counties, Utah. U.S. Geological Survey Scientific Investigations Report 2019-5062.
- McIntosh, J.C., Ferguson, G., 2021. Deep meteoric water circulation in Earth's crust. *Geophys. Res. Lett.* 48.
- Murray, K.E., Reiners, P.W., Thomson, S.N., Robert, X., Whipple, K.X., 2019. The thermochronologic record of erosion and magmatism in the Canyonlands region of the Colorado Plateau. *Am. J. Sci.* 319 (5), 339–380.
- Noyes, C., Kim, J.-H., Person, M., Ma, L., Ferguson, G., McIntosh, J.C., 2021. Geochemical and Isotopic Assessment of hydraulic connectivity of a stacked aquifer system in the Lisbon Valley, Utah (USA), and critical evaluation of environmental tracers. *Hydrogeol. J.* 29, 1905–1923. <https://doi.org/10.1007/s10040-021-02361-9>.
- Nuccio, V.F., Condon, S.M., 1996. Burial and thermal history of the Paradox Basin, Utah and Colorado, and Petroleum Potential of the Middle Pennsylvanian Paradox Formation. In: *Evolution of Sedimentary Basins-Paradox Basin*. USGS Bulletin 2000-O.
- Parry, W.T., Chan, M.A., Beitler, B., 2004. Chemical bleaching indicates episodes of fluid flow in deformation bands in sandstone. *Am. Assoc. Pet. Geol. Bull.* 88 (2), 175–191.
- Pederson, J., Burnside, N., Shipton, Z., Rittenour, T., 2013. Rapid river incision across an inactive fault—implications for patterns of erosion and deformation in the central Colorado Plateau. *Lithosphere* 5 (5), 513–520.
- Porcelli, D., Ballentine, C.J., Wieler, R., 2002. An overview of noble gas geochemistry and cosmochemistry. In: Porcelli, D., Ballentine, C.J., Wieler, R. (Eds.), *Noble Gases in Geochemistry and Cosmochemistry*. In: *Reviews in Mineralogy and Geochemistry*, vol. 47. Geochemical Society, Mineralogical Society of America, pp. 1–19. Chapter 1.
- Rønnevik, C., Ksienzyk, A.K., Fossen, H., Jacobs, J., 2017. Thermal evolution and exhumation history of the Uncompahgre Plateau (northeastern Colorado Plateau), based on apatite fission track and (U-Th)-He thermochronology and zircon U-Pb dating. *Geosphere* 13, 518–537.
- Thackston, J.W., McCulley, B.L., Preslo, L.M., 1981. Ground-water circulation in the western Paradox Basin, Utah. In: Wiegand, D.L. (Ed.), *Geology of the Paradox basin: Rocky Mountain Association of Geologists Field Conference*, pp. 201–225.
- Torgersen, T., 2010. Continental degassing flux of  $^4\text{He}$  and its variability. *Geochem. Geophys. Geosyst.* 11.
- Torgersen, T., 1980. Controls on pore-fluid concentration of  $^4\text{He}$  and  $^{222}\text{Rn}$  and the calculation of  $^4\text{He}/^{222}\text{Rn}$  ages. *J. Geochem. Explor.* 13, 57–75.
- Torgersen, T., 1989. Terrestrial helium degassing fluxes and the atmospheric helium budget: Implications with respect to the degassing processes of continental crust. *Chem. Geol., Isot. Geosci. Sect.* 79, 1–14.
- Torgersen, T., Clarke, W.B., 1985. Helium accumulation in groundwater, I: An evaluation of sources and the continental flux of crustal  $^4\text{He}$  in the Great Artesian Basin, Australia. *Geochim. Cosmochim. Acta* 49, 1211–1218.
- Trudgill, B.D., 2011. Evolution of salt structures in the northern Paradox Basin: controls on evaporite deposition, salt wall growth and supra-salt stratigraphic architecture. *Basin Res.* 23, 208–238.
- Tyne, R.L., Barry, P.H., Hillegonds, D.J., Hunt, A.G., Kulongoski, J.T., Stephens, M.J., Byrne, D.J., Ballentine, C.J., 2019. A novel method for the extraction, purification, and characterization of noble gases in produced fluids. *Geochem. Geophys. Geosyst.* 20, 5588–5597.
- Tyne, R.L., Barry, P.H., Karolytė, R., Byrne, D.J., Kulongoski, J.T., Hillegonds, D.J., Ballentine, C.J., 2021. Investigating the effect of enhanced oil recovery on the noble gas signature of casing gases and produced waters from selected California oil fields. *Chem. Geol.* 584, 120540.
- Wescott, W.A., Hood, W.C., 1994. Hydrocarbon Generation and Migration Routes in the East Texas Basin. *Am. Assoc. Pet. Geol. Bull.* 78, 287–306.
- Young, E.D., Galy, A., Nagahara, H., 2002. Kinetic and equilibrium mass-dependent isotope fractionation laws in nature and their geochemical and cosmochemical significance. *Geochim. Cosmochim. Acta* 66 (6), 1095–1104.
- Zhou, Z., Ballentine, C.J., 2006.  $^4\text{He}$  dating of groundwater associated with hydrocarbon reservoirs. *Chem. Geol.* 226, 309–327.